Observation and calibration strategies for large-scale multi-beam velocity-resolved mapping of the [CII] emission in the Orion molecular cloud

Higgins, R.; Kabanovic, S.; Pabst, C.H.M.; Teyssier, D.; Goicoechea, J.R.; Berne, O.; ... ; Tielens, A.G.G.M.

Astronomy & Astrophysics manuscript no. orion-CII-data-release-paper
November 24, 2021

Observation and calibration strategies for large-scale multi-beam velocity-resolved mapping of the [CII] emission in the Orion molecular cloud*

R. Higgins[1], S. Kabanovic[1], C. Pabst[2], D. Teyssier[3], J. R. Goicoechea[4], O. Berne[5], E. Chambers[6], M. Wolfire[7], S. T. Suri[8], C. Buchbender[1], Y. Okada[1], M. Mertens[1], A. Parikka[6], R. Aladro[9], H. Richter[10], R. Güsten[9], J. Stutzki[1], A.G.G.M. Tielens[2]

[1] I. Physikalisches Institut der Universität zu Köln, Zülpicher Straße 77, 50937, Köln, Germany
[2] Leiden Observatory, Leiden University, P.O. Box 9513, 2300 RA Leiden, Netherlands
[3] Telespazio Vega UK Ltd for ESA/ESAC, Camino bajo del Castillo, s/n, Urbanizacion Villafranca del Castillo, Villanueva de la Cañada, 28692 Madrid, Spain
[4] Instituto de Fisica Fundamental, CSIC, Calle Serrano 121-123, 28006 Madrid, Spain
[5] CNRS, IRAP, 9 Av. Colonel Roche, BP 44346, 31028 Toulouse Cedex 4, France
[6] SOFIA-USRA, NASA Ames Research Center, MS 232-12, Moffett Field, CA 94035-0001, USA
[7] Department of Astronomy, University of Maryland, College Park, MD, USA
[8] Max Planck Institute for Astronomy, Königstuhl 17, 69117 Heidelberg, Germany
[9] Max Planck Institut für Radioastronomie, Auf dem Hügel 69, 53121 Bonn, Germany
[10] German Aerospace Center (DLR), Institute of Optical Sensor Systems, Rutherfordstr. 2, 12489 Berlin, Germany

November 24, 2021

ABSTRACT

Context. The [CII] 158μm far-infrared (FIR) fine-structure line is one of the dominant cooling lines of the star-forming interstellar medium (ISM). Hence [CII] emission originates in, and thus can be used to trace a range of ISM processes. Velocity resolved large scale mapping of [CII] in star forming regions provides a unique perspective on the kinematics of these regions and their interactions with the exciting source of radiation.
Aims. In this paper we explore the scientific applications of large scale mapping velocity resolved [CII] observations. With [CII] observations we investigate the influence of stellar feedback on the ISM. We present the details of observation, calibration and data reduction using a heterodyne array receiver mounted on an airborne observatory.
Methods. A 1.15 square degree velocity resolved map of Orion molecular cloud centred on the bar region was observed using the upGREAT heterodyne receiver flying on-board the Stratospheric Observatory for Infrared Astronomy (SOFIA). The data was acquired using the 14 pixels of the German REceiver for Astronomy at Terahertz Frequencies (upGREAT) observing in an on-the-fly mapping mode. 2.4 million spectra were taken in total. These spectra were gridded into a three dimensional cube with a spatial resolution of 14.1 arcseconds and spectral resolution of 0.3 km/s.
Results. A square degree [CII] map with a spectral resolution of 0.3 km s^{-1}is presented. The scientific potential of this data is summarized with discussion of mechanical and radiative stellar feedback, filament tracing using [CII], [CII] opacity effects, [CII] and carbon recombination lines and [CII] interaction with the large molecular cloud. The data quality and calibration is discussed in detail, with new techniques presented to mitigate the effects of unavoidable instrument deficiencies (such as e.g. baseline stability) and thus to improve the data quality. A comparison with a smaller [CII] map taken with the Herschel/Heterodyne Instrument for the Far-Infrared (HIFI) spectrometer is presented.
Conclusions. Large scale [CII] mapping provides a new window on the kinematics of the ISM. The interaction between massive stars and the ISM is probed via [CII] observations. Spectrally resolving the [CII] emission is necessary to probe the micro physics induced by massive stars feedback. We show that certain heterodyne instrument data quality issues can be resolved by using a spline based technique, and that better data correction routines allow for more efficient observing strategies.

Key words. Instrumentation: spectrometer, ISM: structure, ISM: photon-dominated region (PDR), ISM: bubbles , ISM: individual (Orion), Methods: observational, Far-infrared: ISM

1. Introduction

Massive stars have profound impact on their environment. They ionize and heat the surrounding gas, creating HII and photo dissociation regions (PDRs) (Osterbrock & Ferland 2006; Hollenbach & Tielens 1999). The resulting stellar heating creates over-pressurized regions that will expand into their surroundings (Spitzer 1978) creating large scale ionized gas and photo-evaporative flows (Bedijn & Tenorio-Tagle 1981; Williams & McKee 1997). This expansion may also be assisted by radiation pressure from the massive stars (Krumholz & Matzner 2009; Murray et al. 2010). Besides this radiative feedback, strong stellar winds of massive stars inject mechanical energy into the interstellar medium, sweeping up dense shells of

*Final data cube is available at the NASA/IRSA https://irsa.ipac.caltech.edu/ or at the CDS via anonymous ftp to cdsarc.u-strasbg.fr (130.79.128.5) or via http://cdsweb.u-strasbg.fr/cgi-bin/qcat?J/A+A/

gas, with sizes of some 10 pc (Castor et al. 1975; Weaver et al. 1977). Moreover massive stars will end their life in an explosion that ejects most of their mass at ~10,000 km s^{-1}into their surroundings. This will result in a supernova remnant filled with hot gas that will expand, further sweeping up surrounding material.

Stellar feedback also influences the interstellar medium on large scales as radiative interaction creates a two phase medium characterized by "dense" clouds subtended in a tenuous intercloud phase (Field et al. 1969; Wolfire et al. 1995). The concerted effect of the many supernovae in an OB association will lead to the formation of a collisionally heated, hot inter-cloud phase (Cox & Smith 1974; McKee & Ostriker 1977). These super bubbles may break out of the galactic plane, venting their hot gas into the lower halo (McCray & Kafatos 1987; Mac Low & McCray 1988; Norman & Ikeuchi 1989). This sets up a global circulation of gas over the disk that thoroughly mixes the ISM over large scales.

The radiative and mechanical feedback by massive stars has a strong influence on the star formation efficiency of the ISM (Williams & McKee 1997; Kim et al. 2013). On the one hand, this interaction will erode the molecular clouds in which these massive stars were formed, thus limiting the reservoir of molecular gas from which new stars can form. It has been suggested (Geen et al. 2017; Gatto et al. 2017) that these gas dispersal processes may be one cause for the observed low star formation efficiency of molecular clouds (Zuckerman & Evans 1974; Leroy et al. 2008). On the other hand, the dense swept-up shells can become gravitationally unstable and thus feedback can trigger new sites of star formation (Elmegreen & Lada 1977). On a global scale, galactic outflows limit star formation by removing gas from the disk and this is a key ingredient in cosmological models of galaxy evolution.

Clearly, feedback by massive stars has a profound effect on the phase structure, physical characteristics, and evolution of the interstellar medium of galaxies. Observationally, this feedback has been studied through X-ray emission of the hot gas component in supernova remnants and stellar wind bubbles (Townsley et al. 2003; Reynolds 2017). Such studies provide a direct measure of the thermal energy of hot gas bubbles involved in the expansion. For young supernova remnants, expansion velocities can be measured through Doppler shifts of UV, optical, and infrared emission lines. However, the kinematics and kinetics of the expanding stellar wind shells is more difficult to trace as velocities involved are quite small (1–20 km s^{-1}) and the gas is relatively cool. The [CII] 1.9 THz $^2P_{3/2}$-$^2P_{1/2}$ fine-structure transition provides an ideal probe of these shells. The largely evacuated cavities allow the stellar photons to travel unimpeded and create a PDR of warm (~200 K), largely neutral gas. Except for the densest regions, this PDR gas cools mainly through the [CII] line (Hollenbach & Tielens 1999). Hence, the observed [CII] intensity provides a direct measure of the thermal response of the gas to stellar FUV photons. Moreover, the sub-km s^{-1}spectral resolution of heterodyne receivers allows a detailed study of the kinematics of wind-blown shells.

At 414 pc ((Menten et al. 2007); Gaia), the Orion Molecular Cloud core 1 (OMC 1) is the nearest region of massive star formation and has been observed at a multitude of wavelengths in the minute detail (Bally 2008; O'Dell 2001; Genzel & Stutzki 1989). OMC 1 houses the Orion Nebula Cluster (ONC) of young stellar objects (Hillenbrand 1997; Megeath et al. 2016). The O7V star, Θ^1 Ori C, dominates the ionizing photon flux and luminosity of this cluster (O'Dell et al. 2017). Interaction of this star with its birth site, the Orion Molecular Core 1, has created the M42 HII region (O'Dell et al. 2009) and its associated PDR (Tielens & Hollenbach 1985; Tielens et al. 1993; Goicoechea et al. 2015). The stellar wind from Θ^1 Ori C has excavated a 4-pc diameter cavity, filled with a tenuous, hot plasma emitting at X-ray wavelengths (Güdel et al. 2008). At optical and UV wavelengths, the region is dominated by HI recombination (e.g., Hα, Hβ) and cooling (e.g., [OIII], [OII], [NII]) lines from the ionized gas in the M42 HII region. The near-, mid-, and far-infrared regions of the spectrum are dominated by fine-structure lines of abundant species perched on the strong continuum from warm dust and broad emission features due to fluorescence of polycyclic aromatic hydrocarbon molecules (Peeters et al. 2002). The [CII] 1.9 THz line is one of the brightest transitions in this spectral window (Stacey et al. 1993; Herrmann et al. 1997; Goicoechea et al. 2015) and provides an excellent tracer of the interaction of massive stars and the surrounding swept up dense shell.

In this paper we present the, at present, largest velocity resolved [CII] map. This data set was observed using the upGREAT receiver (Risacher et al. 2016a) mounted aboard the flying observatory SOFIA (Young et al. 2012). The first science results from this project have already been reported by Pabst et al. (2019). Here we present the details of the observing strategy and the sophisticated data analysis necessary to provide the highest quality science data. The paper is split into 5 sections. The observing strategy section details the square degree mapping strategy with upGREAT. The data reduction section discusses the generation of the final data product and goes into some of the details of the procedures necessary to mitigate the effects of data artefacts resulting from unavoidable instrument deficiencies. These are partially unique to a high frequency (> 1THz) heterodyne receiver on board an airborne observatory. The data integrity section compares the upGREAT map with the Herschel/HIFI map of the central Orion region. In addition the repeatability of observations over multiple flights is investigated in this section. The scientific outlook previews some upcoming scientific work on this unique dataset. A summary section closes out the paper with an outlook of upcoming large scale [CII] mapping projects.

This paper is part of a series of papers looking at [CII] in the OMC. This paper focuses on the data acquisition and reduction details. Follow up papers are in preparation (Kabanovic et al. in prep.; Suri in prep.) while some have already been published (Goicoechea et al. 2020; Salas et al. 2019; Pabst et al. 2019, 2020).

2. Observation overview

2.1. upGREAT

The upGREAT* Low Frequency Array (LFA) receiver is a heterodyne dual polarization array with 7 pixels per polarization, 14 pixels in total. The pixels are placed in a hexagonal format with a pixel at the center of the array, with the two polarizations co-aligned on the sky. At 1.9 THz the hexagon side length is ~32 arcseconds, with each pixel having a beam size of 14.1 arcseconds at 1.9 THz. The pixel spacing is approximately 2.3 times the beam size, this is unavoidable and the necessary minimum spacing for a Gaussian optics instrument. This property leads to gaps in the array pixel distribution on the sky and requires elaborate observing schemes to fully sample a given area. Figure 1

*upGREAT is a development by the MPI für Radioastronomie and KOSMA/Universität zu Köln, in cooperation with the DLR Institut für Optische Sensorsysteme.

Pixel	0	1	2	3	4	5	6
LFAV	0.66	0.65	0.62	0.64	0.60	0.66	0.67
LFAH	0.68	0.64	0.61	0.67	0.62	0.67	0.67

Table 1: Average main beam efficiencies over November 2016 and February 2017 flight series.

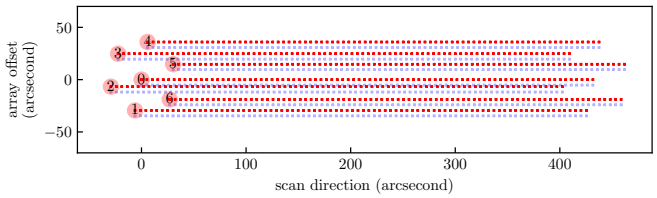

Fig. 1: Overview of upGREAT array pixel layout and an array OTF scan pattern. Red circles show the upGREAT beam size of 14.1 arcseconds rotated to the 19.1° array angle, which gives an equidistant spacing orthogonal to the scan direction between the tracks of the individual pixels along the scan direction. Red dashed line shows a typical 84 dump OTF scan, blue dashed line show the subsequent scan offset at 5.2 arcseconds. Note the pixel positions plotted are actual sky positions from a non perfect alignment hence the larger vertical gap between pixel 0 and 5 compared to pixel 0 and 2.

provides an overview of the pixel layout on the sky during a mapping scan. The upGREAT receiver is coupled to an image rotator which allows the array footprint to be rotated on the sky. Each array of 7 pixels is supplied with the necessary monochromatic signal by an individual local oscillator unit providing frequency coverage from 1.81 to 2.07 THz (Risacher et al. 2016a).

Table 1 provides an overview of the main beam efficiency per pixel. All data presented in this paper is in Rayleigh-Jeans main beam temperatures scale. The overall main beam efficiency is on average 0.65 due to Gaussian coupling losses, illumination of sub reflector and blockage by feed legs, see (Risacher et al. 2016b) for more details. The main beam efficiency is determined at start of each flight series with observations of a known calibration source (typically Mars). After 4 years of LFA operations the average main beam efficiencies between flight series vary within 5%.

The LFA has an average single-sideband (SSB) receiver temperature of 2200K, which for a nominal 10 micron precipitable water vapor atmospheric burden results in a total system temperature of 2600K average over both arrays. The system temperature is defined as the sum of the thermal and receiver noise, for a definition see (Guan et al. 2012). For a more complete discussion of the receiver temperature breakdown see (Risacher et al. 2016b). Figure A.6 provides a summary of the receiver temperature over the course of the project, Figure A.7 shows the distribution of system temperature for both arrays. Figure A.8 shows an example of an individual receiver temperature spectra during a single flight. The local oscillator (LO) was tuned so the OMC line center at a V_{LSR} of 10 km s^{-1}is at an IF frequency of 1.9 GHz in the lower side band. This setting was chosen during preflight receiver tuning as the best compromise between receiver temperature, receiver stability and atmospheric transmission.

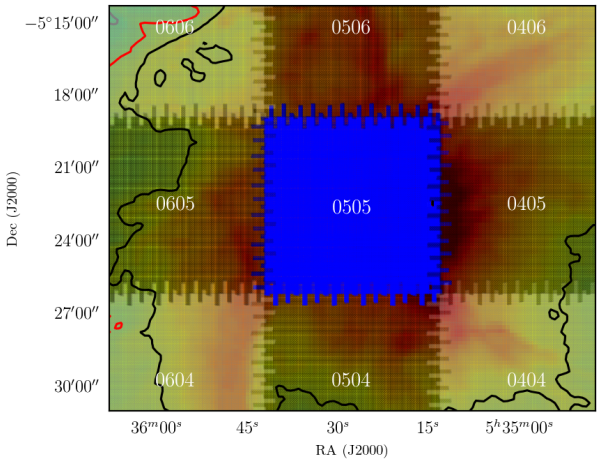

Fig. 2: Overview of tile coverage in array OTF mode. Note the interleaving tile edges.

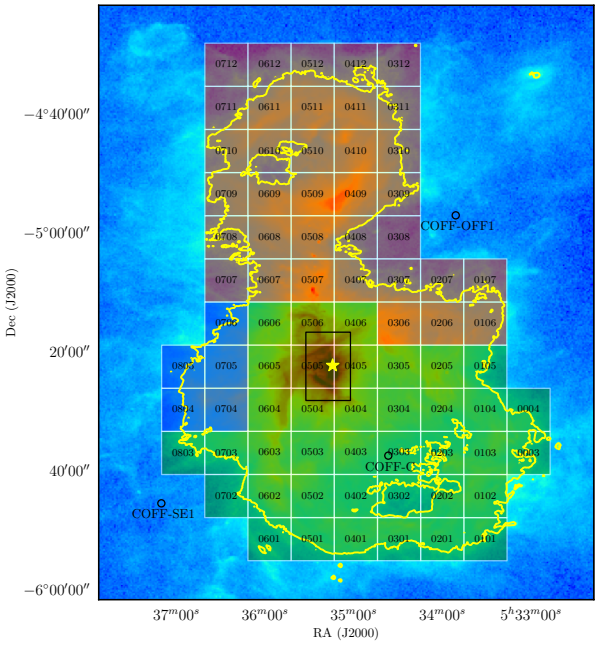

Fig. 3: Overview of 78 tiles and their associated OFF positions. Green tiles are associated with the OFF position COFF-C, blue tiles with COFF-SE1 and red tiles with COFF-OFF1. The background image is a 70 micron from Herschel/PACS. The yellow contour denotes regions at a G_0 of 50 Habing. The HIFI CII map is highlighted with the black box at the center of the map (Goicoechea et al. 2015). Orion KL outflow is marked with a yellow star.

2.2. Observing strategy

The raw data from a typical heterodyne observation is dominated by the instrument response and requires calibration observations to remove these effects and determine the instrument response. The simplest heterodyne observation is made up of 4 phases, an ON phase, an OFF phase and a HOT and COLD calibration phase. The ON phase is an observation of the astronomical target. The OFF phase is normally a region close to the ON target

and ideally devoid of emission at the target frequency. The calibration phase is taken on an internal hot and cold load source with known temperature and receiver coupling. In the case of GREAT, the hot load is at the ambient temperature and the cold load is at a temperature of about 70 K (cooled by a closed-cycle cryostat Stirling cooler). By combining these 4 phases together one can generate a calibrated spectrum, see Guan et al. (2012) for further details.

The duration of the integration in each observing phase, the frequency of the calibration measurements on the hot and cold load, and the pattern of ON- and OFF-source observations are key parameters for the observing strategy. The duration of the hot- and cold-load measurement has to be sufficiently long so that the noise of the hot-cold observation does not significantly contribute to the noise of the calibrated spectra when applying the gain factor; typically, 10 second integrations on the hot- and cold load are sufficient and also imply that the movement of the receiver optics components to steer the beams to the hot- and cold-load, typically of 1 to 2 seconds duration, does not contribute an excessive dead time. The hot-cold measurement needs to be repeated each time the receiver set-up changes, e.g. because of Doppler-tracking of the LO frequency, but also on time-scales, where the gain profile of the receivers slowly drifts. Typically, the hot-cold measurements are repeated every few to ten minutes, also by making use of the necessary interruption of the observations by line-of-sight (LOS) rewinds of the inertially tracking three-axis SOFIA telescope. This cadence is sufficient to correct for worst case gain drifts and Doppler tracking shifts for all possible source positions.

The regular observation of an off-source position is necessary in order to compensate for total power offset drifts, possibly frequency dependent across the receiver reception band, by subtracting the on- from the off-source measurement. By sharing the off-source measurement between several on-source map positions, one can minimize the dead-time on the off-source position, as the minimum signal to noise of the resulting ON-OFF spectra is achieved by making the OFF-source observation $\sqrt{n}$-time longer, where n is the number of on-source positions in each ON-OFF cycle, see (Mangum et al. 2007) for more information. This leads to the raster mapping scheme with a few ONs per OFF, and ultimately to the on-the-fly (OTF) mapping scheme with many (on the order of several 10, up to 100) ONs per OFF. The relative fraction of observing time spent as *dead* time thus decrease $\propto \frac{1}{\sqrt{n}}$.

Thus, in principle, OTF mapping with fast dumps and many dumps per OFF is the most efficient, limited by the data rate that the data acquisition hardware can handle. The ON-OFF cycle has to be short enough, so that the signal drifts, either due to instrument effects, or due to atmospheric changes, do not dominate of the radiometric noise. The stability of a heterodyne receiver can be determined via Allan variance measurements which help determine the time between OFF and ON measurements (Ossenkopf 2009). The spectroscopic stability of upGREAT LFA was determined, based on ideal conditions, to be better than 40 seconds, see Risacher et al. (2016a). For in-flight observation, the stability time is assumed to be 30 seconds given the non-ideal thermal stability of an airborne observatory. This holds for the frequency resolution that is necessary for the Orion [CII] map observations, namely about 0.3 km s^{-1}, resp. 1.9 MHz.

However, for extended sources, the off-source (and the back on-source) telescope slews also take time and they have to be incorporated into the ON-OFF OTF cycle. In practice, this results in OTF dump times of order of a few tenth of a second up to a few seconds and some 10 to 50 ON-source dumps per OTF cycle. The overall on-source efficiency is then up to about 80%.

Note that the stability time, i.e. the time scale on which the drifts (independent of frequency channel width $\Delta\nu$) start to dominate over the radiometric noise (decreasing with the $\frac{1}{\sqrt{\Delta\nu}}$), decreases for broader frequency resolution, e.g. for broad line observations. When the stability time approaches the order of the dead time of the ON-OFF moves, the observing scheme obviously becomes completely inefficient. For compact sources, chopped observations provide a useful alternative, where the ON-OFF movement is done by the wobbling secondary mirror and not by the whole telescope assembly, and is correspondingly much faster. However, the ON-OFF throw is limited to small angles on the sky, for SOFIA to 10 arcminutes maximum. The ON-source observing efficiency in chopped mode, of course, is limited to slightly below 50%, as one has to observed only single pairs of on- and off-source pointings with equal integration time in both, in addition to a small dead time due to the chopper transition time.

Taking the extended nature of the Orion molecular cloud and receiver performance into account the only choice of observing mode was the OTF position switch observation. A further two options of OTF mapping are available for upGREAT. There is the classical OTF mapping and array mapping OTF. Classical mode behaves much like a single pixel observing mode in that a chosen pixel traces out a region in the sky with a fully sampled coverage and all other array pixels follow this pattern. A central core of the map is fully sampled by all pixels while an edge region is under sampled due to the hexagonal nature of the upGREAT array. In contrast, the array mapping OTF mode, illustrated in Figure 1, takes advantage of the hexagonal nature of the array receiver. With careful selection of the angle between the array longitudinal axis and OTF scan direction it is possible with two OTF scans separated by 5.2 arcseconds to cover a fully sampled 72.6 wide arcsecond strip at 1.9 THz (Risacher et al. 2016a). Figure 1 shows a typical array mapping observation with the array tilted to the appropriate angle. If one observes a similar double OTF scan in the orthogonal direction, a fully sampled square region of 72.6 arcseconds is generated. This square region forms the base unit of the array OTF mapping scheme. The OTF array mapping approach allows mapping of large areas in a shorter time while sacrificing signal to noise and pixel redundancy compared to the classical OTF approach. By adding an orthogonal scan to the array OTF mode one can overcome the redundancy short coming by covering each portion of sky with at least 4 pixels, 2 co-aligned H and V pixels in the X direction and then 2 different H and V pixels in the Y direction. Figure 2 shows a typical fully sampled tile with an X and Y scan direction. Furthermore, one can make use of the hexagonal array footprint symmetry by regularly rotating the array by additional multiples of 60 degree in the repetition of observing tiles (see below), thus ensuring that the same area of the sky is observed by different pixels each time, thus equally distributing the pixels over the map area and averaging out any pixel performance differences over the map.

The basic tile is 6 times the base unit tile length of 72.6 arcseconds. Each tile area is covered twice, first in X, and then in Y scan direction. Each OTF scan is 435.6 arcseconds long, an OTF spectrum is taken every 5.2 arcseconds, resulting in 84 OTF spectra per scan. Note that this results in a slightly higher than Nyquist sampling, where the Nyquist sampling as derived from the telescope aperture would be 6.4 arcseconds for a 14.1 arcsecond beam size, so 2.7 samples per beam versus 2.2. (Mangum

Name	RA	Dec	Role
CENTER	$5^h35^m27.6^s$	$-5°22'33.7''$	Map center
COFF-C	$5^h34^m36.5^s$	$-5°37'32.7''$	Green OFF position
COFF-OFF1	$5^h33^m51.0^s$	$-4°57'05.2''$	Red OFF position
COFF-SE1	$5^h37^m10.0^s$	$-5°45'33.7''$	Blue OFF position
FOFF-E	$5^h39^m21.6^s$	$-4°58'29.7''$	Far OFF east
FOFF-W	$5^h31^m15.5^s$	$-5°52'27.4''$	Far OFF west
BAR_PEAK	$5^h35^m20.9^s$	$-5°25'04.8''$	Calibration position

Table 2: Summary of positions used during the project. All map tiles were offset from the CENTER position.

et al. 2007) recommends a sampling rate of at least twice Nyquist sampling to reduce elongation issues to less than 1% in the scanning direction. Elongation is considered in the map making process where a convolution kernel 2-3% larger than the upGREAT beam of 14.1 arcseconds is used to account for this.

In order to stay within the stability time of the system, each OTF dump has an integration time of 0.3 seconds. This results in a total scan duration of 25.1 seconds. An OFF measurement of 2.8 seconds [†] is then taken every OTF scan to minimize system drift effects. The final tile layout is shown in 2, while the final map layout with all tiles is shown in figure 3. The boundaries of the map are set by the estimated UV field of G_0 of 50 Habing. The UV field is determined using the conversion factor from 70 micron to UV field discussed in Goicoechea et al. (2015). The 50 Habing UV region is shown with a yellow contour in figure 3. The final map contains 78 square tiles of side length 435.6 arcsecond.

Figure 2 shows the overlap regions between tiles. The hexagonal layout of the upGREAT LFA array leads to jagged edges at the tile edges. Based on previous heterodyne observations (see HIFI map, Goicoechea et al. (2015)) there is the risk the interface between adjacent tiles will be apparent in the final map. We will show in the reduction section that this wasn't an issue in the final map.

2.3. OFF selection

Figure 3 shows an overview of which tiles are linked to which OFF positions, with different color tiles associated with different OFF positions. In total there are three OFF positions used during the mapping campaign, see table 2 for an overview of the position coordinates. Three OFF positions were chosen to minimize the telescope slew times. During the pilot program in December 2015 dedicated observations were taken against far-OFFs observation to determine the amount of emission from the OFF positions. Clean Far OFF positions were based on previous HIFI observations. It was known in advance that the nearby OFF positions contained some level of emission and would require special processing to remove this emission from the final map. An additional complication in the OFF acquisition is the position angle of the array on the sky. Each map tile is made up of an X and Y OTF scan, the position angle of the array between the X and Y scan differs by 30 degrees resulting in slightly different OFF emission in the X and Y scan directions. This meant that dedicated OFF observation were needed at both the X and Y map angles, as is further explained in detail in section 3.5.

[†] $t_{off} = \sqrt{N_{otf}} * t_{on}$, where N_{otf} is 84 and the scan dump time, t_{on}, is 0.3 seconds, see Mangum et al. (2007) for more details.

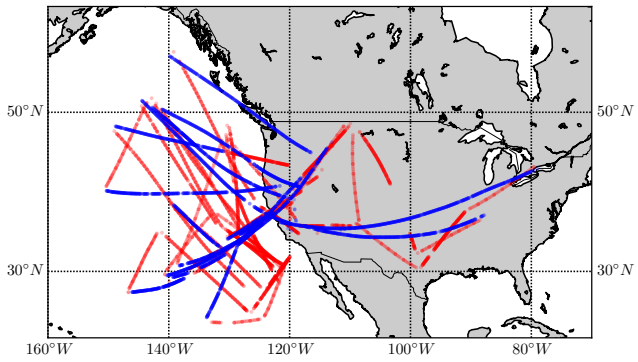

Fig. 4: Overview of the flight plans for the 13 Orion project flights. Each point corresponds to the start of an upGREAT observation block. Blue points highlight the Orion legs while red points show non-Orion flight legs. Each flight returned to Palmdale. The return leg is a not apparent in the map since no observations are taken during the set-up and Palmdale return legs.

2.4. Flight summary

The total project was observed over 13 flights (12 flights for map observations and 1 flight dedicated to calibration and OFF measurements). These flights were divided over 2 flight series, November 2016 and February 2017. Table A.1 provides an overview of the tiles observed per flight. On average 8 tiles were observed per flight. In total 2.4 million spectra were recorded over 42 hours of SOFIA flight time. Figure 4 shows an overview of the flight path with each Orion flight leg highlighted in blue.

3. Data reduction

3.1. Overview

During the observation, raw spectrometer counts from each observation phase (ON/OFF/HOT/COLD) are written to a FITS-file (Pence et al. 2010). The raw data is then converted to antenna temperature using the methods detailed in Guan et al. (2012). In addition to the gain calibration via the HOT-COLD scans, that convert the backend counts to antenna temperature, the atmospheric transmission is determined by fitting an atmospheric model to an OFF-HOT spectrum. The atmospheric transmission corrected data is then written to a GILDAS (Grenoble Image and Line Data Analysis Software/Continuum and Line Analysis Single-dish Software) class file and is further processed within the GILDAS environment (Pety 2005). The data calibration process makes use of the dedicated SOFIA user section (Bardeau et al. 2011) and also the associated array infrastructure available with the GILDAS spectrum data format (Bardeau & Pety 2015).

The first step in the reduction is the removal of the OFF emission contamination (see section 3.5). The next step in the data reduction was the correction of baseline features in the calibrated data. This process was undertaken using a novel scaled spline approach. This will be discussed in detail in section 3.2. The next step in the reduction is the application of the main beam efficiency for each pixel. The spectra are then down sampled to a suitable velocity resolution of 0.3 $km\,s^{-1}$ from the native resolution of 0.04 $km\,s^{-1}$ and then cropped to the velocity range of interest -70 to 85 $km\,s^{-1}$ (in order to cover the [^{13}CII] satellite

transitions, see table 3). A spectral resolution of 0.3 km s^{-1}is a compromise between final data size and without compromising on the average line width expected in the OMC. Generating maps at the native resolution would lead to larger processing times without any added benefit to the astronomical interpretation.

Before proceeding to generate a map, bad data were filtered out based on a number of criteria such as high system temperature or large deviations in noise compared to that expected based on the radiometer equation. Further filters were developed to track Radio Frequency Interference (RFI) (discussed section 3.4) and gain instability (see section 3.3). Finally some spectra were flagged based on a visual inspection of the final map where spectra showed a mismatch with surrounding map pixels.

The final step before map generation is to subtract a mean offset from each spectrum to remove any continuum offsets not corrected during the spline baseline subtraction step. The mean is calculated from a region outside of the main line emission between -10 and 30 km s^{-1}. This approach is prone to RFI effects outside of the -10 to 30 km s^{-1}region that skew the mean offset of a spectrum. This effect can be countered by flagging regions of a spectrum above a given RMS value. This flagging is achieved using the associate array functionality within GILDAS which allows the user to flag channels that are ignored when the baseline offset is calculated (Bardeau & Pety 2015). The associated arrays are a useful addition to the standard GILDAS *ry* array containing the astronomical signal. GILDAS allows the user to associate a number of arrays to the *ry* array. Support is built in for bad channels (known as BLANKED array) and line flagging. These arrays are stored as a 2 bit array to have a minimal memory footprint. Up to 64 bit doubles are supported, which could be useful for storing atmospheric transmission or system temperature alongside the astronomical signal, this will incur a significant storage penalty however.

The final filtered set of spectra are then passed to the map maker within the GILDAS software. This takes all map positions and interpolates them onto a fixed square grid by using a Gaussian kernel based on the beam size of upGREAT at the [CII] transition frequency (~14.1 arcseconds). The final map resolution is 18 arcseconds with a pixel size of 3.5 arcseconds. The pixel size is chosen to fully sample the kernel size and allow for smoother contours in the final map. Channels affected by RFI are weighted down to zero weighting in the map generation step by multiplying the associated array weighting array by the spectrum intensity. Since each pixel of the map is observed by at least 4 upGREAT pixels and RFI affected just a subset of data this selective weight approach was possible. Also the advantage here is that one discards only the affected channels and not the entire spectrum.

The next sections go into more detail of the data processing and discussing the baseline correction, gain instability, RFI mitigation and OFF correction.

3.2. Baseline correction using a scaled spline approach

The average difference between ON- and OFF-source scans in an ideal system should be zero in channels that do not contain ON-source signal. The signal common to both ON- and OFF-source positions, such as the thermal noise from the sky and the receiver intrinsic noise contributions are identical. In practice the unavoidable drifts of system components together with the larger or smaller time lag between the ON- and OFF-source integration leave residual baseline features in the calibrated spectrum.

The standard and commonly accepted procedure to correct for these instrument deficiencies is to fit a polynomial or sinusoidal model to the data outside of the line region. Ideally the instrument effect is a slow changing variation and interpolation under the line region is sufficient to correct the spectrum. However, there is no way to quantitatively justify if this approach is correct. In particular, in sources where the line emission is a significant portion of the spectrum (galactic center, extragalactic sources) this classic approach is limited and can potentially corrupt the underlining astronomical data.

Baseline features come in different families. Careful selection of a model best suited to correcting the baseline feature is crucial to correctly remove instrument effects. A common baseline effect is due to the standing wave pattern that is associated with back-scattering from the secondary mirror which causes a sinusoidal modulation of the continuum level in the spectrum and thus scales with the continuum strength of the observed source. The pattern shape itself is relatively constant and similar for all data of a map; in particular, it is weak for those areas of the source, that do not have a strong continuum. In the case of upGREAT, experience shows that the higher frequency channels are less affected by these secondary standing waves; a scattering cone is installed on the central part of the SOFIA secondary mirror (covering the area corresponding to the part of the primary mirror beam obscured by the tertiary mirror tower and mirror). The dominant baseline structure affecting upGREAT data comes after the signal detection in the intermediate frequency amplification chain.

The back scattering in this case occurs between electrical components in the amplification chain in this case between the mixer and the first amplifier. The period of the associated pattern is a function of the coaxial cable length connecting the two components. Unlike the classic secondary mirror detector cavity, the reflection and transmission properties of the electrical component vary significantly over the IF bandwidth of the mixer leading to a complex residual baseline structure, see Higgins & Kooi (2009) for more details. With the Hot Electron Bolometer (HEB) used for upGREAT, the impedance and hence the mixer reflection properties are dependent on the pump level of the mixer. If there is a small change in receiver Local Oscillator (LO) power during the course of an observation, the mixer impedance state changes during the acquisition of the ON and OFF phase which then leads to non-optimum baseline structure residual. The shape of this baseline structure is complex and varies from upGREAT pixel to pixel. Furthermore some pixels are more sensitive to LO power fluctuations than others. To remove these artefacts from the calibrated data a simple polynomial fit is not sufficient. This is especially a problem for sources where the line emission is a significant portion of the total spectrum (extra-galactic or galactic center observations) and it is difficult to disentangle instrument residuals and astronomical emission. These baseline structures also affect the narrow line emission (5-20 km s^{-1}wide) Orion data, in particular with regard to proper identification of the weak [^{13}CII] satellites (see section 5.6).

One characteristic of a standing wave in the electronics is that it is LO frequency independent (different LO frequencies return the same baseline structure). The shape of the baseline structure is primarily a function of the impedance state of the reflecting elements and the cable length between them, see Chapter 3 in Higgins (2011) for a detailed discussion. In the case of upGREAT the two reflecting elements are the mixer and the first low noise amplifier. This leads to spectra observed minutes apart having similar baseline structure. Using this property it is possible to generate a catalogue of baseline structures from the residu-

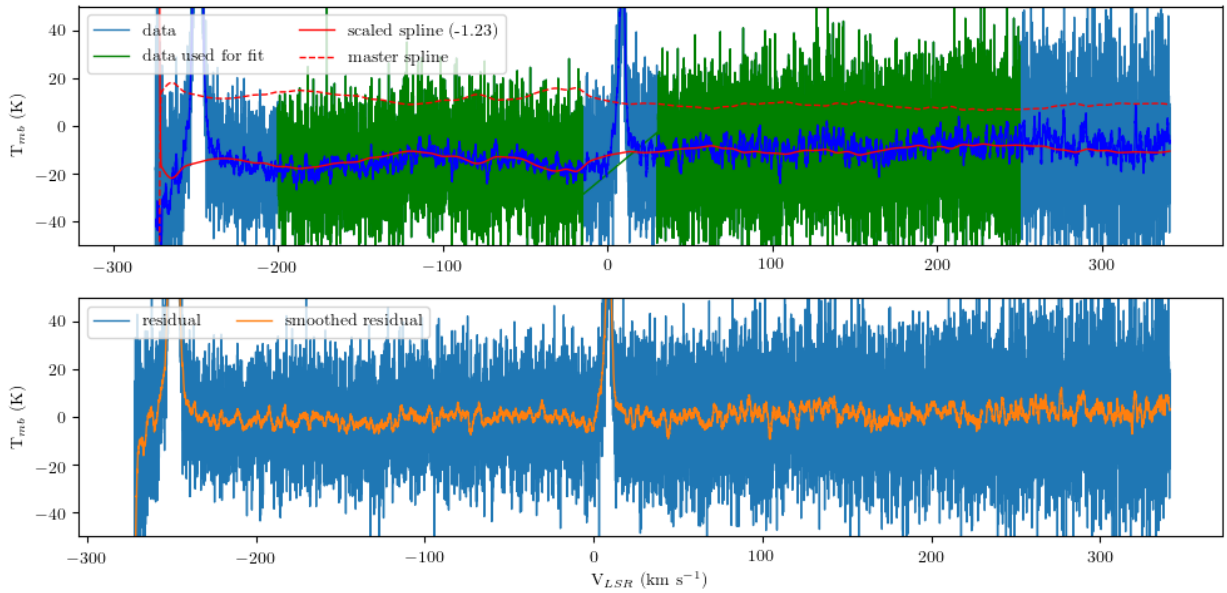

Fig. 5: Example of the spline baseline correction process. The dashed red line is the master spline generated from the residual of 2 OFF sky measurements. The solid red line is then a scaled version of the master spline which best matches the smoothed sky data (dark blue). The green region shows the channel range over which the spline is fitted. The lower panel shows the residual of the spline correction, light blue shows the original data resolution, orange shows a smoothed version of the corrected data.

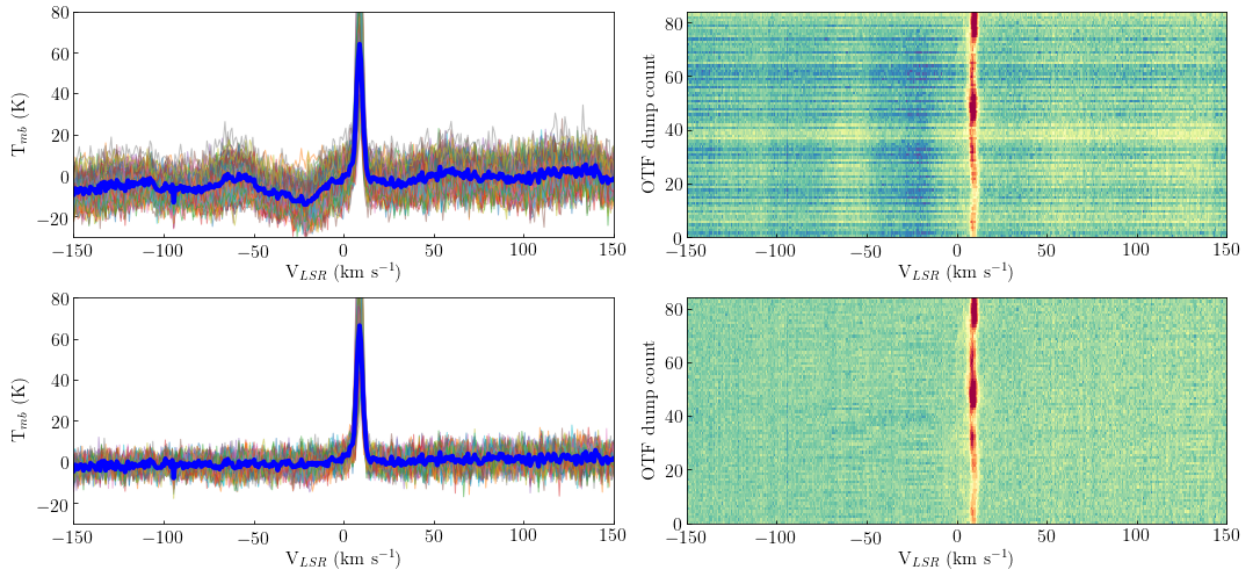

Fig. 6: Example spline baseline correction for a typical OTF scan of 84 dumps length. *Top left panel:* Baseline after standard polynomial order 3 baseline correction with average over 84 dumps shown in dark blue. *Top right panel:* Water fall plot of 84 spectra taken during an OTF scan, note the dip at -25km s^{-1}common to all spectra. *Bottom left panel:* Baseline after spline correction applied, corresponding water fall plot shown on the right hand side. *Bottom right panel:* Water fall map of 84 spectra after spline correction.

als between OFF measurements which can be used to correct the ON-OFF data. With the advantage that the residual OFF spectra are devoid of astronomical emission.

To facilitate the matching of baseline catalogue spectra, each spectrum in the OFF residual catalogue is fitted with a spline profile and the fit parameters are stored in a table. Each ON spectra is then compared to each spectra in the OFF residual spline catalogue. Each spline is scaled to the ON data with the best match determined by the residual with the minimum chi-squared. This is similar to the approach developed by Kester et al. (2014) where they used a Bayesian approach to find the best fit.

Figure 5 shows an example of a individual baseline correction process. The data is first smoothed so the underlying baseline structure is more apparent. This smoothed spectrum is then compared with scaled spectra regenerated from the spline catalogue. The plot shows an example of an OFF residual spectra multiplied by a factor of -1.23 which best matches the ON

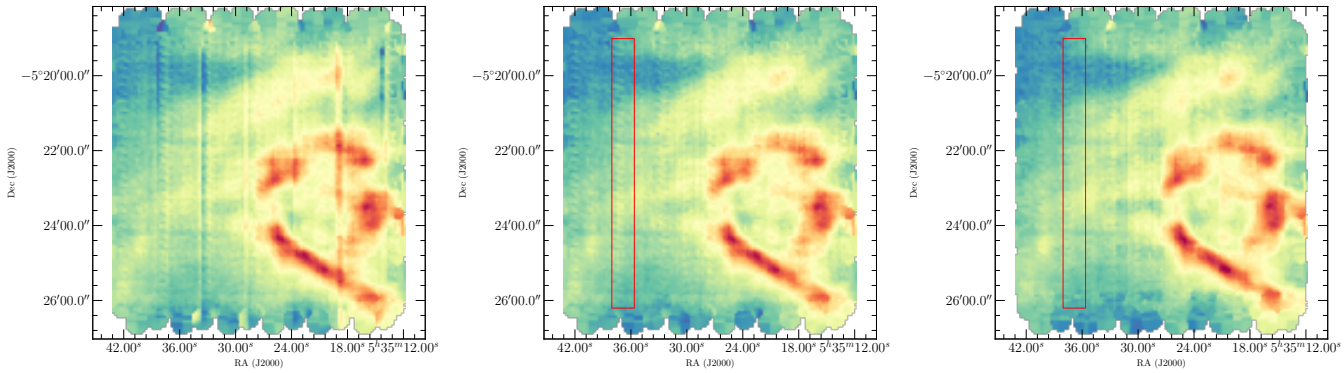

Fig. 7: *Left panel:* Integrated intensity between -5 and 15 km s^{-1} for the center tile using a polynomial order three correction. *Center panel:* Same tile using a spline correction approach. *Right panel:* Using a spline approach and filtering pixels with gain instabilities. The red box in the center and right panels highlights a region of gain instability that shows up as a zipper like artefact in the map that is only apparent after the spline baseline correction (for more details see section 3.3).

calibrated spectra. This scaled OFF residual spectra is then subtracted from the ON spectrum. Figure 6 shows an example of the process applied to a single OTF scan (84 spectra). The waterfall plots on the right hand side best illustrate the nature of the baseline feature. Note the profile has troughs and rises at the same velocity. The only variation in the profile seen over the course of the OTF scan is the scaling. The left hand panels show the individual spectra for each OTF with the average spectra before and after baseline correction over plotted.

This process has no effect on the underlying intensity calibration. Figure A.1 shows the same data shown in Figure 6 but with a comparison to the nearby LFAH2 pixel. The LFAH2 pixel is not affected by data quality issues and provides a good comparison to the spline corrected LFAV2 pixel. It should be noted however than the LFAV2 and LFAH2 pixels are not co-aligned and are offset by 2 arcseconds on the sky so there is some difference in line emission, in this case there is a $\sim$ 5 kelvin peak difference. The difference is maintained before and after baseline correction which gives us confidence that correction method is not affecting the data calibration. To further this point, Another example is shown in Figure A.4 for a galactic center observation, showing the average spectra before and after spline correction. Note the line emission is not discernible for the V0 pixel before correction but afterwards shows a consistent line intensity with the H0 pixel.

The generation of the OFF catalogue doesn't require a special observation mode and the OFFs taken as part of the regular observation process are sufficient. Ideally the OFF catalogue should be generated from OFF spectra nearby in time, up to 30 minutes. This depends on the atmospheric stability but it is possible that atmospheric emission varies between OFF measurements and this can add another dimension of instability to the baseline that isn't receiver related, for example note the large emission between -300 and -200 km s^{-1} in figure 5 which is associated with atmospheric line emission (This region is then duly ignored for baseline fitting). These non-receiver baseline shape will be discarded during the fitting procedure as the regions with variable atmospheric emission lead to large chi-squared residuals in that region of the spectra. Figure A.2 shows an example of an OFF catalogue for the LFAV0 and LFAH0 mixer from a Galactic center project. Note the large variation in baseline shape for pixel V0 while pixel H0 shows relatively flat baselines. Figure A.3 show the spline correction process for this dataset. A spline fitted to the bold blue spectra shown in Figure A.2 is scaled by a factor -1.56 which provides an accurate fit to the baseline shape and recovery of the weak line emission.

Figure A.5 shows the RMS distribution for each map tile of the large Orion map before and after spline correction for 2 different pixels. The RMS is taken over a spectral range of -75 to 80 km s^{-1} with the central line region blanked out. Baseline problems are typically identified for a particular pixel and over a particular time period by a long non-Gaussian tail towards higher values of RMS. After the spline correction the RMS distribution approaches a closer to Gaussian distribution. Pixel LFAV2 and LFAH0 are shown for comparison. LFAV2 is a pixel that had particularly bad baselines and significantly benefited from the spline correction. The LFAH0 pixel has better performance, the RMS distribution before and after spline correction shows no discernible difference.

Figure 7 shows the central tiles of the map with spline baseline correction method and with a typical polynomial third order correction. Note that only part of the map is affected by poor baseline line structure, hence the striped structure in the non-spline corrected map. The third map shows a second processing step which will be discussed in the next section.

The spline fitting and minimization was undertaken using the python/SciPy library(Virtanen et al. 2020). The SciPy library was used from within the GILDAS environment using the pyclass library (Bardeau et al. 2013). The code to fit a spline to data and generate a catalogue of baseline shapes is available at `https://github.com/KOSMAsubmm/kosma_gildas_dlc`. The galactic center data shown in figure A.4 is available as a demo dataset. The repository also contains functions integrating the pandas table (McKinney 2010) and matplotlib plotting (Hunter 2007) libraries into the GILDAS ecosystem via the pyclass interface.

3.3. Gain Instability

Once the baseline issues are resolved, the second order effects become apparent. Figure 7 shows an example of one such effect highlighted with a red box. It appears like a zipper in the map. The effect is not apparent in a single spectrum and only becomes apparent when one looks at the integrated intensity over an OTF scan. Figure 8 shows the corresponding OTF scan in the red box of figure 7. This region of the map was covered by a Y scan with pixels H6 and V6. The integrated intensity for the H pixel shows a smooth profile as the telescope moves through the 435 arcsec-

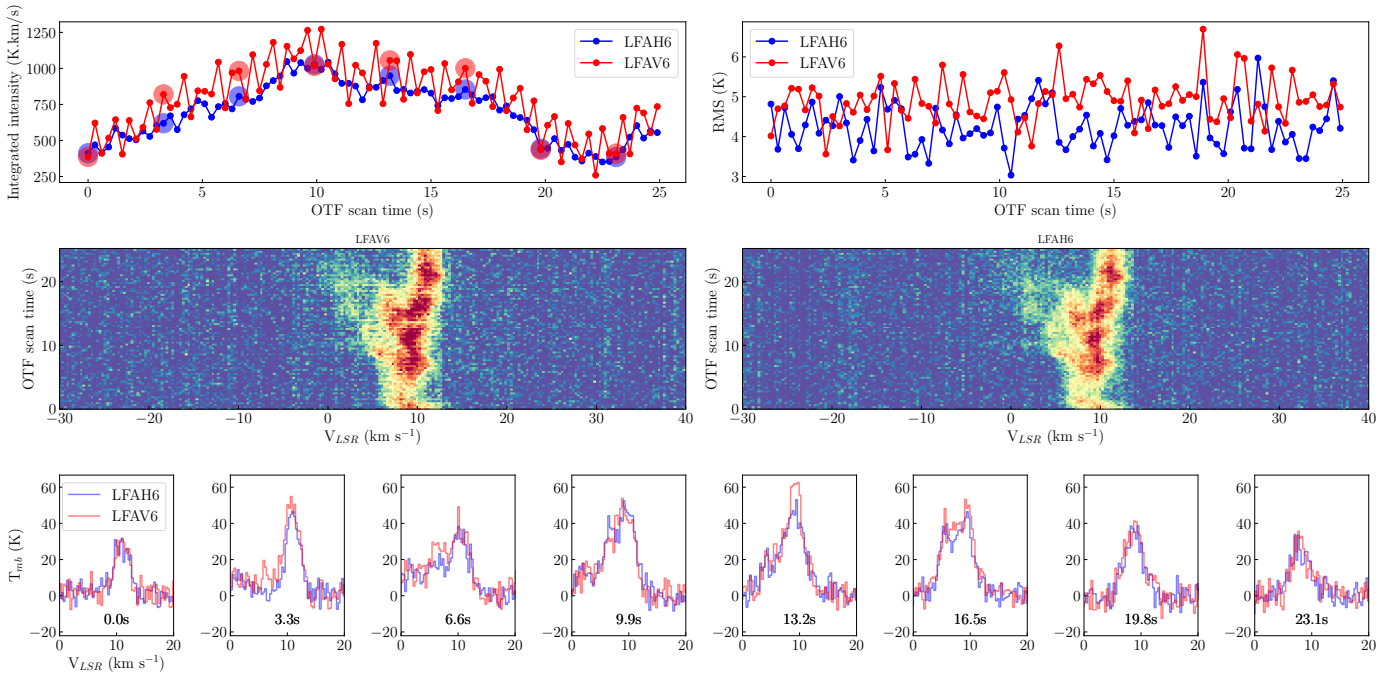

Fig. 8: Example of gain instability seen in pixel LFAH6 for a single OTF scan. *Top left panel:* Integrated line intensity between 0 and 15 km s^{-1} versus OTF dump time. *Top right panel:* RMS over a velocity range from 30-40 km s^{-1}. *Center panel:* Map of 84 spectra associated with a single OTF scan, LFAV6 is shown on the left and LFAH6 is shown on the right. Note the noisy behaviour between adjacent dumps associated with the V pixel not seen in the H pixel. *Bottom panel:* 8 example spectra associated with the solid circles shown top left panel.

.

ond OTF scan. The V pixel shows a similar pattern but with a larger scatter compared with that of the H pixel. The source of this instability can be traced back to a vibration coming from the cryogenic cooler. The cold head, which keeps the mixers at their 4 Kelvin operating temperature, oscillates at a frequency of 1.3 Hz. This vibration modulates the LO power pumping the mixer which causes the mixer pump state to oscillate with the period of the cold head. This behaviour is particularly noticeable in the V array. The baseline features discussed in the section 3.2 are one manifestation of this vibration. Another, more subtle, effect is the modulation of the mixer gain. This is a apparent in figure 8. The integrated line intensity is seen to oscillate during the OTF scan. This effect is most prominent in pixel V6 and to a lesser degree in pixel V2. One expects to see a similar variation in all pixels associated with a given LO, however this is not the case. Further investigations are needed to understand the origins of this effect.

Unlike the baseline effects seen in the previous section, the gain variations are difficult to detect and mitigate. For this dataset we have developed a filter to detect when this gain instability is present. Gain instability is not seen for all flights or pixels. The filter looks at the variability in integrated intensity for a given OTF scan. By running a rolling standard deviation over bins of 5 OTF dumps, one sees a clear distinction between stable and unstable regime. Each OTF scan is processed using these criteria and if an OTF scan goes over a given threshold the data is flagged and not included in the map reduction. Figure A.11 shows a rolling standard deviation of the integrated intensity time line shown in figure 8. Note the V6 pixel shows a higher variability compared to the H6 pixel.

One would expect a gain instability to show up in the spectrum noise but this is not the case. The top right panel of figure 8 shows the RMS over a 30-40 km s^{-1} window. It would be expected that a gain variation would affect the mixer sensitivity and hence the measured RMS of the spectra. There is no apparent correlation between the variations in integrated intensity and spectrum RMS.

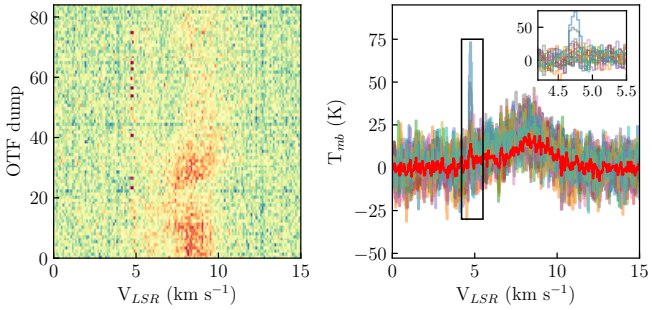

Fig. 9: Example interference from a mobile phone during the flight of 20170209. *Left panel:* Example of 84 dump OTF scan showing RFI (red dots) at 4.75 km s^{-1}, line emission is seen centred around 9 km s^{-1}. *Right panel:* Example spectra showing RFI effects at 4.75 km s^{-1}. *Right inset:* Zoom on RFI emission, the emission is multiple channels wide and has a maximum peak of 75 Kelvin.

3.4. Radio interference during flight

RFI are parasitic man-made radio emission coming from terrestrial sources which can corrupt astronomical observations

(Fridman & Baan 2001). RFI is a major problem for low frequency (< 5 GHz) observatories such as LOFAR (Offringa et al. 2013), SKA (Ellingson 2004) and the Effelsberg 100m (Flöer et al. 2010). It is also becoming an issue for higher frequencies with the onset of radars in self driving cars (up to 300GHz, see Köhler et al. (2013)) and new satellite internet systems (Starlink from SpaceX, see McDowell (2020)). SOFIA is also prone to a plethora of aviation RFI sources such as distance measuring equipment (DMEs), instrument landing systems (ILS) and Secondary Surveillance Radar (SSR) observed between 900 to 1200 MHz. Ideally this shouldn't be an issue for a high frequency radio receiver (> 1THz) such as upGREAT but since it down converts to frequencies between 0 and 4GHz it is also susceptible to RFI effects.
Figure 9 shows an example of RFI effects seen in Pixel H3. An intermittent spike, multiple channels wide, is observed over the course of an 84 dump OTF scan. In the final map, the RFI then shows up as a scratch like artefact at a given velocity channel. RFI effects are fortunately just seen for two of the fourteen upGREAT pixels, namely pixels H3 and H6. Although the cause is not understood, we speculate that this may be due to a leaky IF connector in the IF chain of these pixels. The RFI shown in figure 9 corresponds to a frequency of 1.9 GHz, which corresponds to a mobile phone frequency. The example shown was observed during flight number 372 (2017/02/09).

Fortunately this signal was only detected on this flight thus affecting 10% of the total data. Other RFI signals are also detected, such as bluetooth at 2.4 GHz and a number of aircraft related signals, but they do not fall close to the [CII] (or [^{13}CII]) line emission.
As mentioned in the overview section, RFI can corrupt baseline fitting methods and also can contaminate other data when the corrupted channels are convolved with healthy channels from pixels. One option would be to ignore the affected spectrum completely but this discards data that is useful except for the 10 channels affected. Another option would be to replace the affected channels with an equivalent noise however since the RFI effects shown in figure 9 are within the line emission velocity range, this could contaminate the line emission in a more subtle way. Fortunately the GILDAS software team have implemented a method to weight the significance of a given spectral channel in the map making process using an associated array. Using these methods it is possible to flag an RFI affected channel and then weight these channels down to zero when generating the final map. With this approach it is possible to ignore the RFI affected channels but retain the other healthy channels from the affected spectra. The crucial component in this process is the associated array support in GILDAS. This allows the user to store an additional array in parallel to the intensity array. For this reduction a dedicated "RFI associated array" was used to track outlier channels in a spectrum. RFI affected channels were flagged using a rolling standard deviation and a threshold generated from the local RMS. The code to perform this operation is available in the *despike* method in the same github repository as the spline correction code.

Great efforts are made by the SOFIA observatory (pre-flight briefing info, on-board request to switch off RFI sources) to mitigate RFI but given the prevalence of radio emitting devices today, It is difficult to police completely. To mitigate these effects an RFI detector will be deployed on future flights to detect bluetooth, WiFi and mobile phones signal. This system will alert observatory staff who can locate the RFI source.

3.5. OFF correction

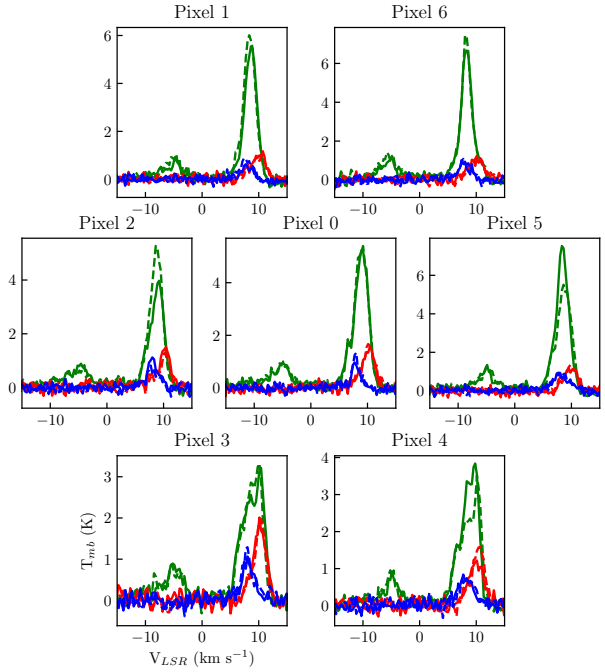

Fig. 10: Overview of emission from the 3 OFF positions for H array pixels. Note each position is observed at the X and Y scan direction orientation (Y is shown in the dashed line in plot). The colors correspond to the color shown in the tile overview in figure 3 (Blue is COFF-SE1, Green COFF-C and Red COFF-OFF1).

As mentioned in section 2.2, one of the concerns in undertaking such a large map of a large scale extended source, requiring far off OFF positions, was the effect of slew time to the OFF position on overall data quality. A further issue was the change in atmospheric transmission between observation phases when the angular distance between the ON and OFF phase is large. It was decided to minimize the effect of slew times (and therefore distances) by using three OFF positions around and inside the map region[‡]. The drawback to this approach is that all chosen OFF positions are contaminated with [CII] emission. Dedicated observations were undertaken of the OFF position coupled to a known far-OFF position free of emission (see position summary in table 2). The resulting spectra of the OFF emission are shown in figure 10. Note that at each pixel/position combination there are 2 spectra corresponding to the OFF positions of each pixel resulting from the array angle first for the X (solid line) and then for the Y (dashed line) scan direction. Rotating the array on sky takes a few seconds of time, the array angle is kept constant between the OTF scan and OFF position acquisition to improve observing efficiency. Note that for some positions there are significant differences between the OFF spectra taken with the array angles for the X and Y scan (see pixel 5 position COFF-C for an example).

[‡]The approach of using nearby OFFs has since been shown to be conservative, follow up maps of the Orion region with the upGREAT receiver have used the FOFF-West (see table 2) without any adverse effects to the data. When base line quality is poor it is possible to recover data using the spline methods demonstrated here.

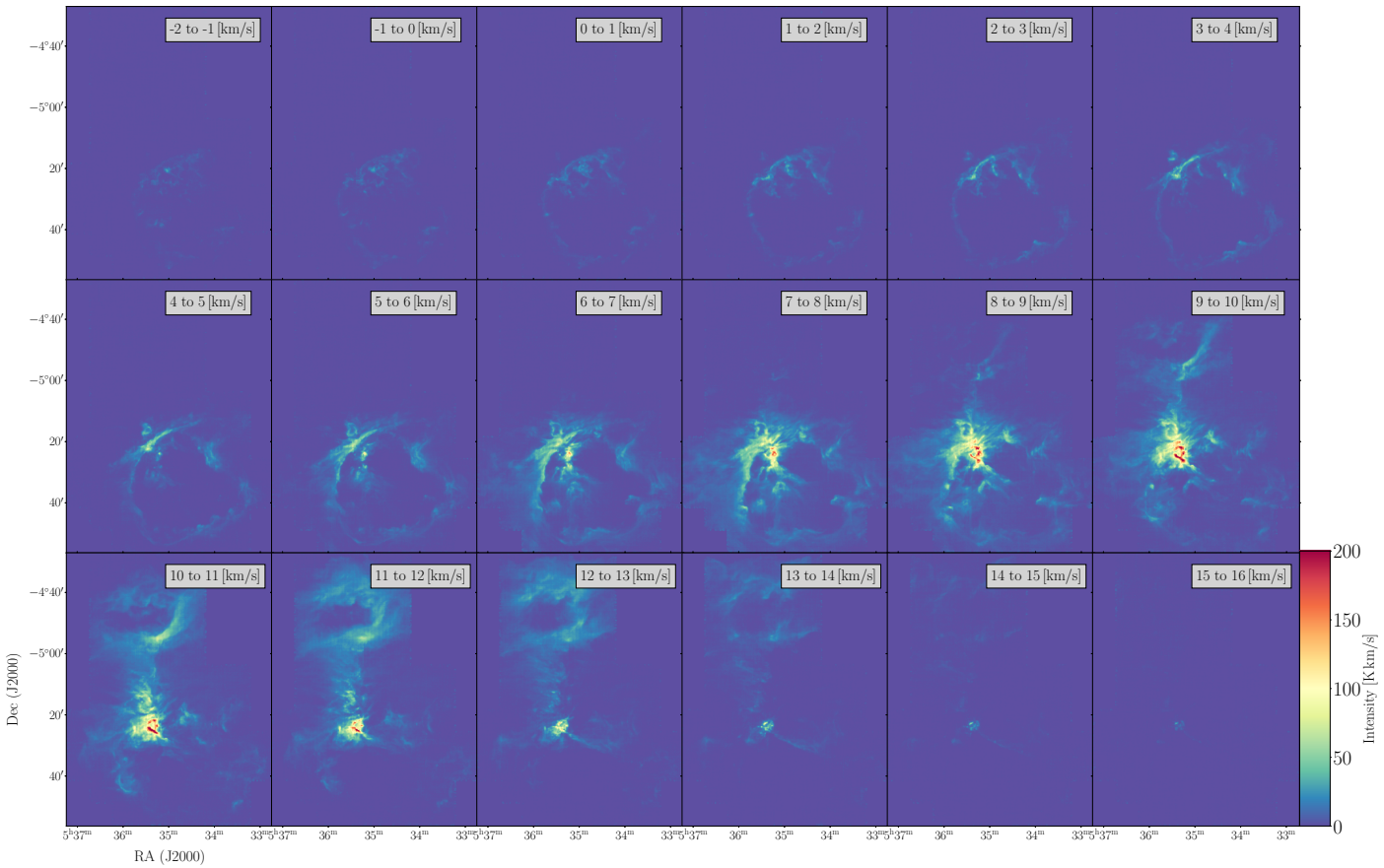

Fig. 11: Final velocity cube generated with a Gaussian kernel of 18 arcseconds projected onto a grid of 3.5 arcseconds square pixels.

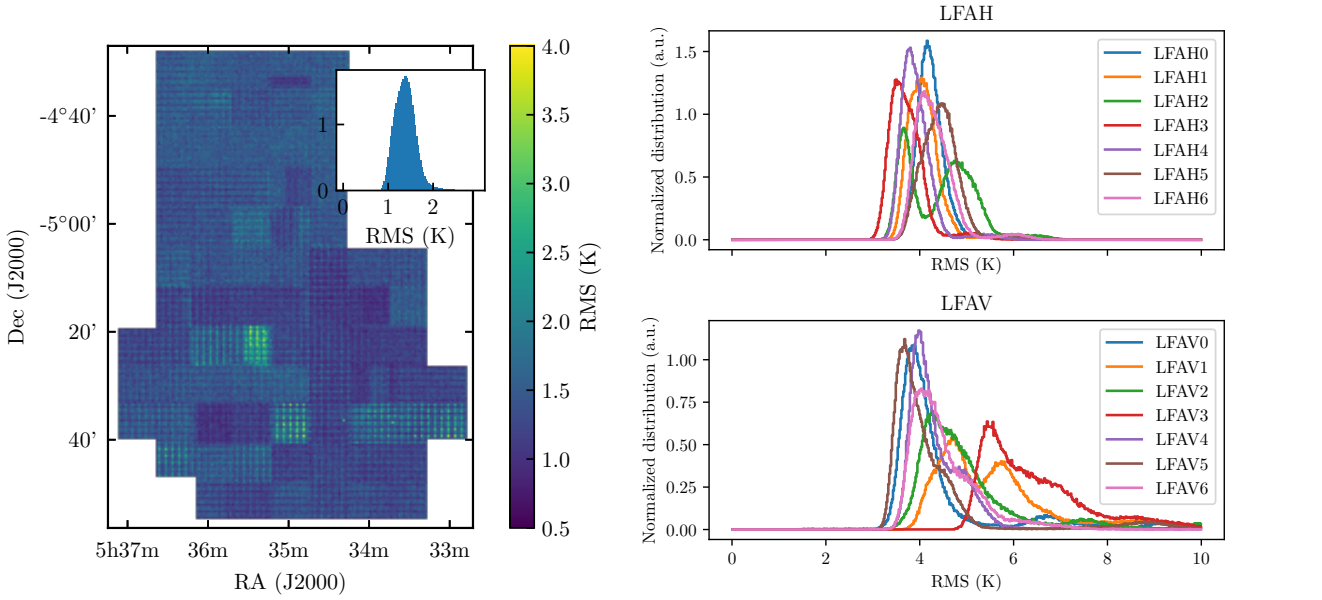

Fig. 12: *Left panel:*Distribution of RMS over final map. RMS taken over a line free range from -50 to -20 km s^{-1}with a 0.3 km s^{-1}spectral resolution. *Left inset panel:* RMS map shows a histogram of the distribution of RMS over the entire map with a peak value of 1.63K. *Right panel:* Distribution of spectrum RMS before map generation with a 0.3 km s^{-1}spectral resolution. Note some pixels have 2 peaks (V1,H2) or a trailing tail (V3) in their distribution indicating a change in RMS performance over the two flight series.

OFF contamination is a common effect when mapping extended sources. This manifests itself as an apparent absorption dip in a spectrum and over the entire map. The standard data reduction procedure is to add the contaminated emission back to the On sky emission. This procedure is significantly more complex with an array receiver as the OFF contamination is unique to each pixel. This is further complicated as the direction of the scan also has a unique OFF emission. So in total for the Orion [CII] map there are 84 unique OFF spectra, for 14 pixels at 3 OFF positions and in 2 scan directions. Figure A.9 shows as an example the average spectrum over a tile before and after OFF emission correction for each pixel.

3.6. Summary

Channel maps of the final data product are shown in figure 11. The final map is generated using the *xy_map* function in GILDAS convolved with a kernel of 18 arcseconds and a pixel size of 3.5 arcseconds. Figure 12 shows an overview of the spectrum RMS before and after the map generation. The RMS distribution of the individual 0.3 second OTF dumps is shown on the right hand side of figure 12, Note the performance difference between the H and V arrays. The broadness of the distribution for the V array is related to a changing performance of pixels in later flights in the series. This is best illustrated in figure A.6 which shows an increasing system temperature towards later flights. Figure A.5 shows the variation in RMS for the different tiles, note the increasing RMS for the V2 pixel toward the northern part of the map.

The final map RMS is shown in the left hand panel of figure 12. The first feature of the map is the stripe feature moving through the map. This indicates some of the non-uniform performance of the pixel over the course of the flight series, which is also seen in the receiver temperature summary plot (figure A.6) and also in the RMS distribution before deconvolution. These variations in performance are difficult to avoid and are still a topic of investigation within the upGREAT team. This can be a combination of changing LO performance and illumination of the array, since the array response doesn't degrade uniformly over the flight series. Stripes also show regions where spectra were dropped due to other performance issues, such as RFI and gain variations discussed in previous sections.

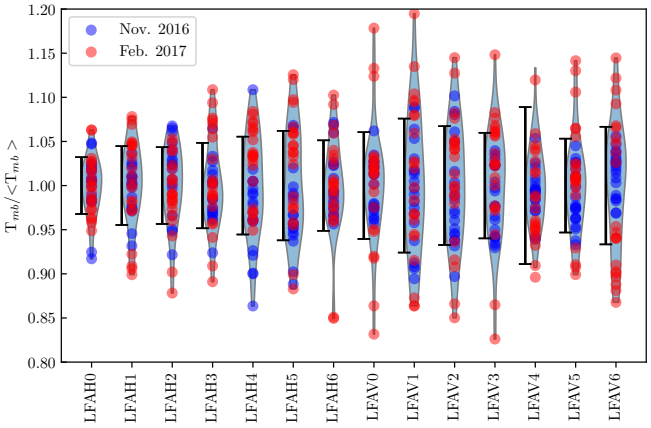

Fig. 13: Mean normalized integrated intensity of Orion bar reference observations per pixel. Red dots represent individual observations, black bars the standard deviation. The blue shaded region is a violin plot of the Kernel density estimation.

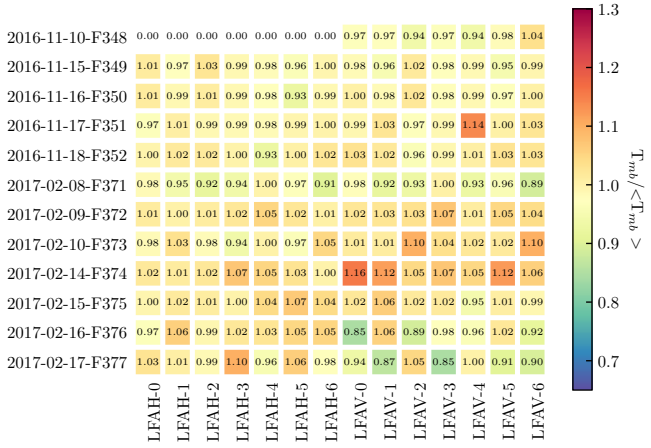

Fig. 14: Heatmap of mean normalized integrated intensity of Orion bar observations over all flights and pixels.

4. Data integrity

4.1. Consistency between flights

The large scale OMC [CII] map was the first time a project of this scale was undertaken with the upGREAT instrument. The lessons learned from the careful data reduction as described here are of particular importance as they pave the path for the now ongoing SOFIA [CII] mapping legacy programs (Schneider et al. 2020; Pineda et al. 2020). The observations were spread over 13 flights and 2 flight series (November 2016 and February 2017) providing a unique opportunity to test the repeatability of upGREAT observations. There are a number of factors that could affect the repeatability of upGREAT observations varying from the atmospheric calibration, pointing repeatability and receiver stability. Furthermore there are additional factors that affect the repeatability of observations between flight series, such as the repeatability of the receiver mounting on the telescope flange. The main concern from the scientific goals of the project was the repeatability of observations from flight to flight. There was a concern that the overlap between tiles could be an issue based on previous experiences from HIFI (Goicoechea et al. 2015) and IRAM 30m (Berné et al. 2014). This would require additional data reduction to correct the instrument response from tile to tile.

This necessity and importance to monitor the upGREAT performance was identified in advance and a reference observation was scheduled for each flight. A region on the Orion bar (array centred on 5h35m20.90 −5°25′04.8″) was chosen and a single point total power observation of 3 minutes total duration was observed at least once on each flight, 20 observations in total were observed, the position is shown in Figure 18. Figure A.10 shows an overview of each of these reference observations for each pixel. Figures 13 and 14 provide a summary of the normalized integrated line intensity over a -5 to 15 km s^{-1} window for all pixels across these reference observations. Normalization was achieved by dividing each spectra by the average line emission over all reference observations for that pixel. Ideally all points should be close to 1.

Taking the standard deviation of each pixel and averaging over all pixels returns a repeatability of +/- 6% between flights. If we break this up further we see that the H array has repeata-

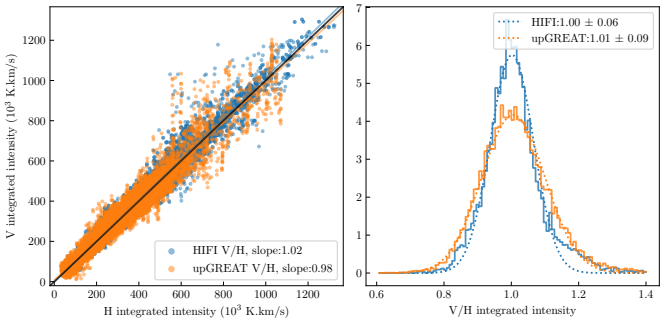

Fig. 15: Comparison of line intensity between the H and V polarization over a velocity range of -5 to 15 km s^{-1}. Data is shown for upGREAT and HIFI. *Left panel:* V polarization is plotted against H polarization. The legend shows the slope of a linear fit through the origin. *Right panel:* Histogram of V/H integrated intensity, the legend shows the fitted offset and width of a Gaussian profile.

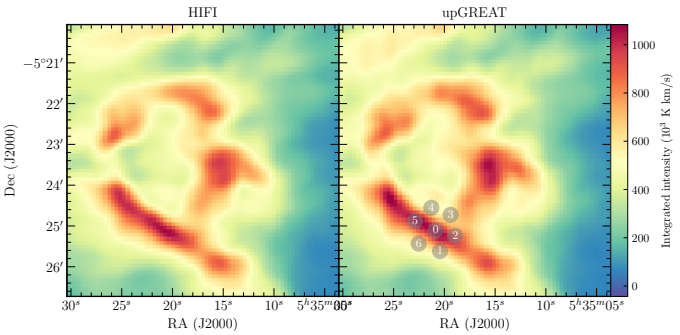

Fig. 16: Side by side plot of HIFI and upGREAT data. Both maps are generated with 22 arcsecond mapping kernel, both datasets are in main beam antenna temperature. The integrated intensity between -5 and 15 km s^{-1}is shown. The array positions highlighted in grey shows the location of the Orion bar consistency observation discussed in Section 4.1.

bility of close to 5% while the V array is closer to a 7% repeatability. This is consistent with the other trends seen in the data quality where the H array was seen to perform better than the V array. Varying performance between the two arrays could be linked to different LO performance between the 2 arrays. We observe an increase in receiver temperature towards later flights, see figure A.6. However these effects are not uniform across the array which suggests that some pixels are more sensitive to LO performance than others. This could be due to the method used to split the LO signal between the 7 mixers. The single beam LO output signal is divided into 7 beams via phase grating, small changes in alignment of the phase grating and mixers can affect the illumination of each pixel differently. The degradation of receiver temperature over the course of a flight series points to an LO performance issue however. This resulted in the LFAV LO been shipped back to the manufacturer for maintenance. After this maintenance a more uniform performance across the two arrays was seen.

4.2. Consistency between H and V array

An additional check of the instrument performance is the consistency between the H and V integrated intensity. Figure 15 shows the H integrated intensity plotted against the V integrated intensity for the central region of the map shown in figure 16. Plotting the V against the H data provides an overview of the linearity between the 2 polarizations. This linearity holds up to highest intensities observed in the map. The histogram of V divided by H polarization provides a statistical measure of the consistency between the two polarizations. The upGREAT histogram is centred at 1.01. The linear fit to the V versus H plot shows a slope of 1.02 between V and H intensity, indicating that the upGREAT V array is on average 2% brighter than the H array. For consistency, the HIFI V and H performance (the comparison between HIFI and SOFIA/upGREAT data is discussed in detail in the next section) is also plotted. This shows slightly better performance however this is just a two pixel comparison. The line fit to the HIFI H and V data shows a similar 2% difference between polarizations. It should be noted that the upGREAT data is a comparison between two seven pixel array and it is expected to have more scatter given the different main beam efficiencies and associated uncertainties (see table 1).

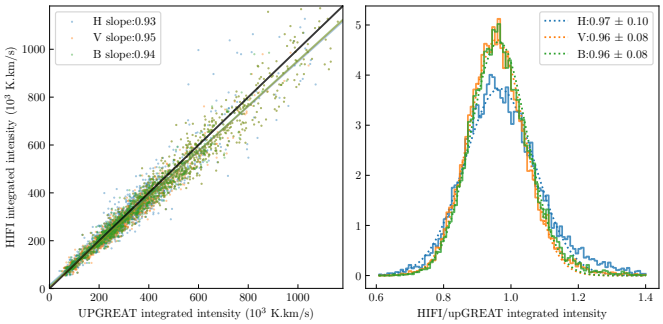

Fig. 17: *Left panel:* Integrated intensity from HIFI and upGREAT maps plotted against each other. 3 upGREAT maps are shown, separate maps for H and V polarizations and a map with both polarizations together. The HIFI map is generated from both polarizations. *Right panel:* The distribution of the HIFI map divided by upGREAT maps with a Gaussian fit. Plot legend shows the fitted Gaussian width and offset.

4.3. Intensity comparison with HIFI map

Another factor that affects the repeatability of observations between flights is the atmosphere. The atmospheric transmission calibration process makes a number of assumptions, e.g. on the layering of the atmosphere above the aircraft, on the stability of the atmospheric transmission during the ON-OFF cycle, and on the validity of the atmospheric model over time. This can lead to an over or under estimation of the atmospheric transmission leading to inconsistency between flights. This section looks to address this issue by comparing the upGREAT [CII] Orion map with one taken by the Herschel/HIFI spectrometer (Goicoechea et al. 2015; de Graauw et al. 2010). As a satellite mission, HIFI was free of the atmospheric contribution and so provided a unique dataset to compare with the upGREAT map.

Figure 16 shows a side by side comparison of the HIFI and upGREAT maps. Both maps used a Gaussian kernel of 22.1 arcseconds on grid of 6 arcseconds. The larger mapping kernel was used to account for the under sampled nature of the original HIFI map. Figure A.12 shows a similar comparison but with a mapping kernel of 18.1 arcseconds. Note the blocky nature of the HIFI map is due to the fact that the OTF map was not Nyquist sampled and has on average a grouping of spectra every 10 arc-

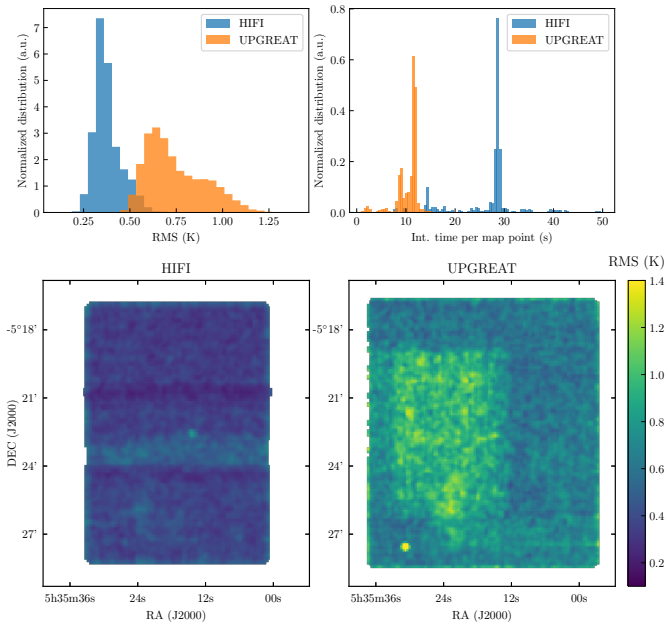

Fig. 18: RMS comparison between HIFI and upGREAT between -50 and -20 km s^{-1}. *Top left panel:* Histogram of RMS map shown in bottom panels. *Top right panel:* Histogram of integration time per map point. *Bottom panels:* Spatial distribution of RMS for HIFI and upGREAT. The region of higher RMS in the upGREAT map is from the first flight when the LFAH LO wasn't available. Dark horizontal bands in the HIFI map show lower RMS regions which correspond to the overlap between the map tiles.

seconds due to the load chop observing mode, see Figure A.13 for a comparison of spectra distribution between upGREAT and HIFI. From a visual inspection of figure 16 both maps show a good spatial correlation.

The bottom panels give a more quantitative view on the 2 datasets. The integrated intensity of each HIFI map pixel is plotted against the same upGREAT map pixel. For completeness, 3 upGREAT maps are generated, one with the H array, V array and then both arrays combined (labeled B). The resulting cloud of points is fitted with a linear curve going through zero. In an ideal situation when both instrument measure the same intensity the fitted slope would be 1 (see the black line in the plot). In this case the upGREAT intensity is on average 4% brighter than the average HIFI map. The histogram on the right panel of figure 17 shows the distribution of the HIFI intensities divided by those of upGREAT. This provides an additional view of the 2 datasets and shows that each HIFI and upGREAT map pixel is on average within a factor of 0.96 of each other.

HIFI had a calibration of accuracy of 10% based on extensive pre-flight and in-orbit testing (see HIFI Handbook), UpGREAT states a calibration accuracy of ±20%(Risacher et al. 2016a). The good correlation between the 2 dataset provides a vote of confidence in the atmospheric calibration code and overall calibration of the upGREAT receiver.

4.4. Performance comparison with HIFI map

Figure 18 shows a comparison of the instrument noise between the two instruments. The final map RMS from HIFI and upGREAT are shown in the lower panels. The HIFI map has a lower RMS compared to the upGREAT map as HIFI has a longer integration time per map point. The top right panel in figure 18 shows the distribution of integration time per map point. upGREAT has a better overall system temperature compared to HIFI, however the longer integration time for the HIFI map leads to a lower RMS.

Figure A.7 shows an overview of system temperatures from HIFI and upGREAT, upGREAT has an average single side band receiver temperature of 2600K versus 3600K for HIFI. Even with the additional noise from the atmosphere, upGREAT has a factor 1.4 lower system temperature than HIFI. From the radiometer equation this difference means an upGREAT pixel is twice as efficient as a HIFI pixel or alternatively a single upGREAT pixel can achieve the RMS as a HIFI pixel in half the time. When the factor 7 difference in pixel count, 2 for HIFI compared to 14 for upGREAT, upGREAT can map a region to the same RMS 14 times quicker than HIFI would take, which is consistent with a similar analysis of the CII Horsehead map in (Risacher et al. 2016a).

Another dimension in the comparison between HIFI and upGREAT is the observing efficiency, nominally defined as the fraction of on source time over the total observation time. A direct comparison between HIFI and upGREAT Orion maps isn't possible given the significantly different observing modes used. Overall one would expect the observing efficiency of an airborne observatory to be higher than that of a satellite given the higher accelerations and slews speed possible on SOFIA, Herschel having a maximum slew speed of 0.1 degrees per second compared to 1 degree per second for SOFIA. However other factors also play a role such as co-ordination between the instrument and telescope. A detailed discussion of observing efficiency is beyond the scope of this paper. Efficiencies quoted in the Herschel Explanatory Supplement Volume I (section 4.3.2.2) of between 30 to 50% are largely consistent with SOFIA/upGREAT observations.

The large leap in progress from HIFI to upGREAT was only achievable using an airborne telescope where the instrument team can upgrade the receiver after each flight series and continuous push forward the development. This rate of progress is not possible with satellite based instruments where the receiver is not accessible in orbit and the design is frozen early in the development process. Note that during this project upGREAT had an LO performance issue during the first flight that was quickly resolved for the next flight. Furthermore the degrading performance of the LO during the last 2 flights of the project was resolved after the flight series in time for the next upGREAT campaign. In addition to the hardware flexibility, the software system is also flexible and continuously updated to improve observing efficiencies and track data quality issues (for example RFI effects on board).

5. Scientific Outlook

The interstellar medium (ISM) and its interaction with massive stars are central to the evolution of star forming galaxies. Mechanical and radiative energy input by massive stars stir up the interstellar medium and heat interstellar gas. This controls the characteristics (density and temperature) of the phases (diffuse clouds, warm intercloud, and hot intercloud) of the interstellar medium, sets the thermal pressure of the gas, and the distribution of the gas over these phases (Field et al. 1969; Wolfire et al. 1995; McCray & Snow 1979; Weaver et al. 1977). Stellar feedback also govern star formation as ionized evaporative flows,

stellar winds, and supernova explosions will disrupt molecular clouds thereby stopping star formation (negative feedback) while at the same time gas is compressed in shells, promoting gravitational instabilities (positive feedback) (Elmegreen 2011; Elmegreen & Lada 1977; Hopkins et al. 2014). The relative importance of these feedback processes and their dependence on the characteristics of nearby massive stars and the surrounding ISM is not well understood.

Radiative energy input by massive stars also controls the emission spectrum of star forming galaxies. EUV ($h\nu > 13.6$ eV) photons ionize the gas and heat it to $\sim$ 7500K. This photo-ionized gas cools through optical and UV collisional excited lines and through (H) recombination lines. These processes are well understood and HII regions and their properties have been extensively studied on galactic and extragalactic scales (Osterbrock & Ferland 2006). H gas is transparent to FUV photons ($6 < h\nu < 13.6$ eV) but trace species with low ionization potentials can still be ionized. The neutral HI gas is heated through photo-electrons from polycyclic aromatic hydrocarbon molecules and small dust grains. These photons travel thus largely unimpeded through HII regions, creating a layer of warm gas in so-called photo dissociation regions (PDRs) separating the ionized gas from the surrounding molecular cloud as well as, on the scale of a galaxy, creating the cold neutral medium (diffuse clouds) (Hollenbach & Tielens 1999). Of the relevant trace species, carbon is the most abundant one and [CII] is the main ion in FUV illuminated gas. This neutral HI gas cools through far-infrared fine structure lines of e.g., [CII] at 1.9 THz. As the dominant cooling lines can only be observed with airborne or space based platforms, much less is known about the properties of PDRs.

Recent observations reveal that much of the molecular gas mass is in a form not probed by CO (so-called CO-dark molecular gas), its standard tracer (Grenier et al. 2005; Planck Collaboration et al. 2011). For diffuse clouds, hydrogen is atomic and carbon is ionized ([CII]). In CO-dark molecular gas, hydrogen is in H2 but [CII] rather than CO is the dominant form of carbon (Visser et al. 2009; Wolfire et al. 2010). The HI and CO-dark phases have so far eluded detailed characterization, because the main tracer of the diffuse ISM, the HI 21 cm line, does not constrain the physical conditions of the gas (e.g., temperature, density) well and optical and UV absorption line studies, which are good probes of the physical conditions, are limited to pinhole experiments towards bright, nearby stars with only low column densities of gas. As a result, the physical conditions of CO-dark molecular gas and its relationship to other phases in the ISM are not well known. This CO-dark molecular gas is heated by far-UV photons from massive stars through photo-electrons from large molecules and very small grains (Bakes & Tielens 1994) and cools through the [CII] 1.9 THz line (Wolfire et al. 2010).

Observations of regions of massive star formation in the [CII] 1.9 THz line carry the promise of providing much insight in all of these aspects of the interaction of massive stars with their surroundings and the structure and characteristics of the ISM. Here, we will briefly summarize the anticipated results of the [CII] square degree survey of Orion. Section 5.1 discusses mechanical feedback aspects, including the Veil bubble created by the stellar wind of θ^1 Ori C and the Spitzer-type expansion of M43 and NGC 1977. Section 5.2 highlights the radiative heating of PDR gas by FUV photons in the Orion region. Section 5.3 discusses the relationship of [CII] and CO emission in the Veil bubble. In section 5.4, we touch upon the interaction of radiative and mechanical energy input on the filamentary structure of molecular clouds and the effects of star formation. In section 5.6, the synergy of [CII] 1.9 THz observations with radio recombination lines of carbon is illustrated. Finally, in section 5.6, we describe the effects of optical depth on the [CII] 1.9 THz emission through observations of the [^{13}CII] isotopologue.

5.1. [CII] observations and mechanical feedback from massive stars

The large [CII] data set at high spectral resolution enables a systematic study of the large scale kinematics of the region (Pabst et al. 2019, 2020). In the [CII] data several expanding structures can be identified; three of them being parsec-scale bubbles affected by stellar feedback by the respective central stars. Specifically, the data reveals that the shell structure surrounding the hot gas within the Extended Orion Nebula, which dominates the morphology of photometric images, is indeed part of a coherently and rapidly expanding shell, whose dynamics is controlled by the stellar wind of the most massive Trapezium star, θ^1 Ori C. The results show that the mechanical energy from the stellar wind is converted very efficiently into kinetic energy of the swept-up shell and, rather than photo-ionization and evaporation, dominates the disruption of the Orion molecular core 1 (Pabst et al. 2019). The HII regions, M43 and NGC 1977, are also associated with expanding shells. These HII regions are powered by less massive stars – NU Ori and 42 Orionis, respectively with feeble stellar winds. In contrast to the Veil surrounding M42, for these regions, the thermal expansion of the warm ($\sim$7500K) ionized gas drives the expansion and the shell dynamics and the disruption of these regions (Pabst et al. 2020).

The [CII] line is one of the brightest far-infrared cooling lines of the ISM and has been proposed as a valuable tracer of star formation across cosmic time scales. The Orion [CII] map provides a valuable data set that can be used to better understand the origin of [CII] emission and its relation to other gas and dust tracers. Specific correlations that can be studied include the relation between [CII] emission, IRAC 8 micron emission, PACS 70 micron emission, total FIR emission, and CO line emission (Pabst et al 2021). Using large-scale data sets allows us to study these correlations across several orders of magnitude and relate their dependency to local physical conditions.

Analysis shows that the [CII] emission correlates well, but non-linearly, with the 8 micron PAH and 70 micron dust emission. This results in a so-called [CII] deficit in regions characterized by warm dust. For Orion, this deficit is caused by a decreased heating efficiency in UV bright regions, an increased importance of other cooling lines, and the contribution of deeply embedded star formation to the far-IR dust emission (Pabst et al 2021; Higgins et al 2021, both in prep.).

5.2. [CII] observations and radiative feedback from massive stars

The [CII] line is a key diagnostic for analysing the heating and physical conditions in the neutral gas (e.g., Kaufman et al. 2006, Pabst et al. 2017). For moderate density photo dissociation regions, and for the bulk of the molecular cloud surface, the [CII] line is the dominant gas coolant. In thermal equilibrium, the [CII] line measures the gas heating regardless of the exact heating process. Whether by radiative heating via photoelectric ejection of electrons from grains as expected for photo dissociation regions, or by mechanical heating from shocks or turbulence, the heating rate is measured by the [CII] line. The ratio of [CII] to

the infrared continuum, [CII]/L_{IR} is a measure of the fraction of radiative energy that is converted to gas heating and is expected to be $0.1 - 1\%$ for PDRs. The theoretical heating rate is a function of $G_0 T^{1/2}/n_e$ where G_0 is the incident far-ultraviolet radiation field and n_e the electron density. We can use the true heating rate as measured by [CII]/L_{IR} to calibrate the theoretical prediction.
Large scale mapping allows for a continuously varying distribution of heating rates, from the dense gas, and intense radiation fields found near the Trapezium cluster to the lower density and lower radiation fields found in the outer edges of the molecular cloud.

While generally the fainter outer edges of molecular clouds are overlooked as a source of [CII] emission when in fact they might dominate the [CII] emission on large scales (Abdullah et al. 2017; Abdullah & Tielens 2020). [CII] observations of extragalactic objects typically sample regions of massive star formation on a scale size of ∼400 pc.

Likely, the [CII] flux from these regions is also dominated by the emission from PDR surfaces on molecular clouds illuminated by moderate radiation fields. When combined with large scale maps of the infrared continuum and the CO (2-1) from the IRAM 30m (PI: Goicoechea) along with theoretical PDR modelling tools (Pound & Wolfire 2008), the [CII] maps provide a measure of the gas temperature, density, and incident far-ultraviolet field strength across the cloud. Analysis shows that the thermal gas pressure scales with the incident radiation field to the power 3/4, as expected for pressure equilibrium between photo-ionized gas and the surrounding PDR (Pabst et al 2021, in prep).

5.3. Relationship of [CII] emission and the large scale molecular cloud

In order to obtain the molecular emission counterpart to [CII], we have started to expand previous ^{12}CO and ^{13}CO (2-1) maps of the central region of Orion A taken with the IRAM 30 m telescope (see Berné et al. 2014). The new maps cover more extended and diffuse CO-emitting regions and are part of a ∼165 h Large Program "Dynamic and Radiative Feedback of Massive Stars" (PI: J. R. Goicoechea). These maps have angular and spectral resolutions of 11″ (≃4,500 AU) and 0.25 km s^{-1}respectively (thus, comparable to those of our [CII] 158 μm map). Thanks to the wide bandwidth of the EMIR receivers it is possible to map lines from ^{12}CO, ^{13}CO, C^{18}O, and other species simultaneously (for details, see Goicoechea et al. 2020).

A combined analysis of velocity-resolved [CII] 158 μm and CO maps at such a high spatial resolution provides a powerful diagnostic tool to study the radiative and mechanical feedback of massive stars. While this kind of analysis has been previously pursued at arcmin^2 scales to probe the interaction between UV radiation from massive stars and their natal molecular cores, see e.g., Goicoechea et al. (2015) for OMC-1 or Pabst et al. (2017) for the Horsehead nebula, much less was known about their square-degree spatial distribution. This large-scale emission samples entire star-forming complexes, their vast (perhaps "CO-dark") surrounding halos, and the swept-up material blown away in the form of expanding shells. Such a coherent C$^+$ and CO data base, used in tandem with archival photometric images of the MIR PAH and FIR dust emission, allows us to quantify the role of UV radiation and stellar winds in great detail. While photometric images do not reveal the gas kinematics of the expanding shells, photo-evaporative flows and hydrodynamical instabilities at molecular cloud interfaces, this is a unique aspect we investigate with these maps. In particular, by studying the C$^+$ and CO emission at velocities different to those of OMC, we can search for any faint molecular emission outside the star-forming cloud: in the swept-up material of the shells, at the edges of HII regions, or in the form of small globules that may lead to the formation of very low mass stars (Goicoechea et al. 2020).

PDR models show that the [CII]/CO (2-1) line intensity ratio depends on physical conditions (G_0 and $n_{\rm H}$). Indeed, the [CII]/FIR vs. CO/FIR relation is used to infer these parameters, not only in local star-forming regions but also toward distant star-forming galaxies (e.g., Stacey et al. 2010). With more than 2 million [CII] 158 μm and CO spectra (and measurements of the far-IR dust emission) toward regions of Orion in which G_0, $n_{\rm H}$, and A_V vary by orders of magnitude, we can accurately calibrate the diagnostic power of the [CII]/CO intensity ratio. More broadly, we use these [CII] 158 μm and CO (2-1) maps to observationally constrain the gas physical conditions, not only G_0, $n_{\rm H}$, and T_k, but also to characterize the gas turbulence and the associated non-thermal contribution to the total pressure balance.

5.4. [CII] emission and the filamentary structure of molecular clouds

The unique spatial and kinematic information that the [CII] map encompasses allow for a comprehensive look into the nature of the filamentary structure in a cloud engulfed by stellar feedback. In an ongoing effort, we are working on a detailed comparison of large scale ^{13}CO and C^{18}O emission (Kong et al. 2018) and [CII] emission maps towards a number of filaments that were previously identified by (Field et al. 1969; Suri et al. 2019). This study, for the first time, reveals the PDR nature of the filaments, their fate in an irradiated cloud, and their relationship to ongoing star formation (Suri et al. in prep).

5.5. Probing PDRs with [CII] 1.9 THz line and carbon radio recombination lines

The physical properties of the atomic and "CO-dark" molecular gas are largely unknown due to the faintness of their probes; e.g., carbon radio recombination lines (CRRLs). Using multiple CRRLs, well spread in frequency, the gas temperature and density can be precisely determined e.g., (Oonk et al. 2017). The analysis of CRRLs can be greatly aided through the combined use of [CII] and CRRLs e.g., (Natta et al. 1994; Tsivilev 2014; Salas et al. 2017). The large area covered by this [CII] survey enables the joint analysis of these lines, from sub parsec to parsec scales, through a synergy with radio telescopes such as ALMA and LOFAR (Salas et al. 2019). This analysis demonstrates that the thermal pressure in the [CII] layers of the PDR in the surface of OMC-1 exceeds that of the ionized gas in the HII region. The strong pressure gradient towards us from the self gravitating core OMC1 to the PDR surface, to the ionized gas, to the hot plasma, to the foreground Veil nebula is at the basis of the evaporative "champagne" flow of the ionized gas (Pabst et al. 2019).

5.6. [^{13}CII] Emission and [CII] Optical Depth Effects

In contrast to the single [^{12}CII] $^2P_{3/2} \rightarrow {}^2P_{1/2}$ transition the [^{13}CII] emission splits into three hyperfine transitions, due to the unbalanced spin of the additional neutron. The location and relative intensity of the [^{13}CII] hyperfine components are shown in Table 3, (Ossenkopf et al. 2013; Guevara et al. 2020).

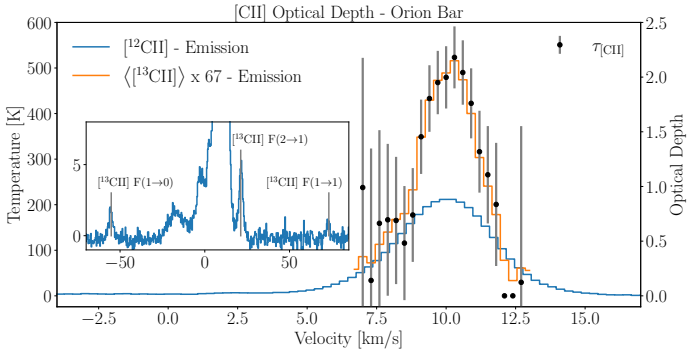

Fig. 19: Averaged [^{12}CII] and [^{13}CII] emission originating from the ridge of the Orion Bar. The blue spectrum shows the [^{12}CII] line and the orange spectrum shows the velocity corrected [^{13}CII] emission averaged over the three hyperfine components and multiplied by 67, the carbon isotopic ratio in Orion (Langer & Penzias 1990). The black data points with error bars show the determined optical depth for each velocity channel, which are above unity around the peak of the line [^{12}CII]. The inner panel shows the three [^{13}CII] hyperfine transitions lines detected alongside the [^{12}CII] line.

Table 3: [^{12}CII] fine structure and [^{13}CII] hyperfine transition parameter.

Transition line	Weight		Freq.	Velocity offset	Relative intensity
	g_u	g_l	ν [GHz]	$\Delta v_{F\to F'}$ [km/s]	$s_{F\to F'}$
[^{12}CII] $^2P_{3/2} \to ^2 P_{1/2}$	4	2	1900.5369	0	1
[^{13}CII] F = 2 → 1	5	3	1900.4661	+ 11.2	0.625
[^{13}CII] F = 1 → 0	3	1	1900.9500	- 65.2	0.250
[^{13}CII] F = 1 → 1	3	3	1900.1360	+ 63.2	0.125

The weak [^{13}CII] emission from the three transition lines require a low spectral rms and a flat baseline structure over a large velocity range ±100 km/s to disentangle the emission from the noise floor. Thus, recovering 'bad' spectra using the novel spline approach by removing baseline features such as drifts, standing waves, etc. and therefore reducing the overall spectral noise are crucial for the [^{13}CII] analysis.

However, the detection of the three [^{13}CII] satellites requires a high signal to noise, much larger that the signal to noise for a given map pixel. The square degree [CII] map allows averaging over arcmin size regions, This results in a greatly improved S/N ratio in the average spectra, facilitating the detection of the isotope emission. The velocity resolved [CII] spectrum averaged over the Orion Bar is shown in Fig. 19. We observe the [^{12}CII] at 10 km/s and the three hyperfine transitions. The strongest [^{13}CII] F(2 → 1) line is shifted by 11.2 km/s from the [^{12}CII] line. This close line is often affected by the wing of the main isotope and therefore not useful for an analysis. The second strongest component is sufficiently far away from the main component, −65.2 km/s but has only 25 % of the total intensity, see Table 3.

The simulation of [^{12}CII] and its isotope [^{13}CII] enables us to determine possible optical depth effects in [CII] cloud emission. Previous studies, e.g. Graf et al. (2012); Ossenkopf et al. (2013); Guevara et al. (2020); Okada et al. (2019), have shown that the [^{12}CII] line can be heavily affected by optical depth effects. Thus, the observed [^{12}CII] intensity or line shape doesn't necessarily reflect the extent of [CII] emission at this position which further highlights the necessity of velocity resolved [CII] observations.

A comparison of the line intensities and shape between [^{12}CII] and [^{13}CII] can reveal if the main component is affected by optical depth effects. The optical depth of the ionized carbon atom can be determined by (Guevara et al. 2020):

$$\frac{T_{mb,[^{12}CII]}(v)}{T_{mb,[^{13}CII]}(v+\Delta v_{F\to F'})} s_{F\to F'} = \frac{1-\exp(-\tau(v))}{\tau(v)} \alpha \quad (1)$$

with the carbon abundance ratio in Orion $\alpha = 67 \pm 3$ determined by Langer & Penzias (1990) and the relative intensity $s_{F\to F'}$ of the hyperfine transition of the ionized carbon isotope.

The [^{12}CII] line and the [^{13}CII] line scaled by the carbon isotopic ratio are plotted in Fig. 19. We observe that the scaled [^{13}CII] overshoots the [^{12}CII] emission indicating optical depth effects as observed by Ossenkopf et al. (2013) in the Orion Bar. The velocity resolved optical depth is shown by the black data points with error bars. The optical depth increases toward the peak of the spectrum, reaching a maximum value of $\tau_{[CII]} = 2.2 \pm 0.3$. Integrating both spectra between 7 − 13 km/s gives us an averaged optical depth for the Orion Bar of $\langle\tau_{[CII]}\rangle = 1.3 \pm 0.1$ similar to the value previously determined by Ossenkopf et al. (2013) using [CII] data obtained with Herschel/HIFI.

As the analysis of the ionized carbon spectrum in the Orion Bar has shown, the observed [CII] spectra might be affected by optical depth effects, which could affect their observed intensity and shape. An unbiased in-depth study of the [CII] optical depth effects across the [CII] map is underway using tools to group similar regions together to increase the signal to noise (Kabanovic et al. in prep.).

6. Summary

In this paper we have introduced the largest velocity resolved map of [CII] observed so far. We described the observing strategy and data reduction. The usage of a catalogue of splines to remove baseline artefacts was demonstrated. The observed data was compared to a similar smaller map taken with the Herschel/HIFI spectrometer. The HIFI and upGREAT data agree to within 4% of each other. The techniques discussed here will benefit upcoming large scale mapping projects such as the SOFIA Cycle 8 legacy project Feedback (Schneider et al. 2020) and the GUSTO balloon mission (Bernasconi et al. 2019).

The latter section of the paper discusses the scientific possibility of this dataset. The scientific topics discussed will be expanded into standalone articles. The final map shown in figure 11 is available from the NASA infrared archive (IRSA).

Acknowledgements. This work is based on observations made with the NASA/DLR Stratospheric Observatory for Infrared Astronomy (SOFIA). SOFIA is jointly operated by the Universities Space Research Association, Inc.(USRA), under NASA contract NAS2-97001, and the Deutsches SOFIA Institut (DSI) under DLR contract 50 OK 0901 to the University of Stuttgart. This work is carried out within the Collaborative Research Centre 956, subproject [A4], funded by the Deutsche Forschungsgemeinschaft (DFG) – project ID 184018867. We thank the Spanish MICIU for funding support under grant AYA2017-85111-P.

References

Abdullah, A., Brandl, B. R., Groves, B., et al. 2017, ApJ, 842, 4
Abdullah, A. & Tielens, A. G. G. M. 2020, A&A, 639, A110
Bakes, E. L. O. & Tielens, A. G. G. M. 1994, ApJ, 427, 822
Bally, J. 2008, Overview of the Orion Complex, ed. B. Reipurth, Vol. 4, 459
Bardeau, S. & Pety, J. 2015, IRAM Memo 2015-4: Introducing Associated Arrays in CLASS, Tech. rep.

Bardeau, S., Pety, J., & Guilloteau, S. 2011, CLASS User Section, Tech. rep.
Bardeau, S., Reynier, E., Pety, J., & Guilloteau, S. 2013, PYGILDAS: Interleaving Python and GILDAS, Tech. rep.
Bedijn, P. J. & Tenorio-Tagle, G. 1981, A&A, 98, 85
Bernasconi, P. N., Walker, C. K., KUlesa, C., & Goldsmith, P. 2019, in AGU Fall Meeting Abstracts, Vol. 2019, A33Q–2940
Berné, O., Marcelino, N., & Cernicharo, J. 2014, ApJ, 795, 13
Castor, J., McCray, R., & Weaver, R. 1975, ApJ, 200, L107
Cox, D. P. & Smith, B. W. 1974, ApJ, 189, L105
de Graauw, T., Helmich, F. P., Phillips, T. G., et al. 2010, A&A, 518, L6
Ellingson, S. W. 2004, Experimental Astronomy, 17, 261
Elmegreen, B. G. 2011, in EAS Publications Series, Vol. 51, EAS Publications Series, ed. C. Charbonnel & T. Montmerle, 59–71
Elmegreen, B. G. & Lada, C. J. 1977, ApJ, 214, 725
Field, G. B., Goldsmith, D. W., & Habing, H. J. 1969, ApJ, 155, L149
Flöer, L., Winkel, B., & Kerp, J. 2010, in RFI Mitigation Workshop, 42
Fridman, P. A. & Baan, W. A. 2001, A&A, 378, 327
Gatto, A., Walch, S., Naab, T., et al. 2017, MNRAS, 466, 1903
Geen, S., Soler, J. D., & Hennebelle, P. 2017, MNRAS, 471, 4844
Genzel, R. & Stutzki, J. 1989, ARA&A, 27, 41
Goicoechea, J. R., Pabst, C. H. M., Kabanovic, S., et al. 2020, A&A, 639, A1
Goicoechea, J. R., Teyssier, D., Etxaluze, M., et al. 2015, ApJ, 812, 75
Graf, U. U., Simon, R., Stutzki, J., et al. 2012, A&A, 542, L16
Grenier, I. A., Casandjian, J.-M., & Terrier, R. 2005, Science, 307, 1292
Guan, X., Stutzki, J., Graf, U. U., et al. 2012, A&A, 542, L4
Güdel, M., Briggs, K. R., Montmerle, T., et al. 2008, Science, 319, 309
Guevara, C., Stutzki, J., Ossenkopf-Okada, V., et al. 2020, A&A, 636, A16
Herrmann, F., Madden, S. C., Nikola, T., et al. 1997, ApJ, 481, 343
Higgins, D. R. 2011, PhD Thesis: Advanced optical calibration of the Herschel HIFI heterodyne spectrometer
Higgins, R. D. & Kooi, J. W. 2009, Society of Photo-Optical Instrumentation Engineers (SPIE) Conference Series, Vol. 7215, Electrical standing waves in the HIFI HEB mixer amplifier chain (SPIE), 72150L
Hillenbrand, L. A. 1997, AJ, 113, 1733
Hollenbach, D. J. & Tielens, A. G. G. M. 1999, Reviews of Modern Physics, 71, 173
Hopkins, P. F., Kereš, D., Oñorbe, J., et al. 2014, MNRAS, 445, 581
Hunter, J. D. 2007, Computing in Science & Engineering, 9, 90
Kabanovic, S., Higgins, R., Stutzki, J., et al. in prep.
Kester, D., Avruch, I., & Teyssier, D. 2014, in AIP Conference Proceedings, Vol. 1636, American Institute of Physics, 62–67
Kim, C.-G., Ostriker, E. C., & Kim, W.-T. 2013, ApJ, 776, 1
Köhler, M., Hasch, J., Blöcher, H. L., & Schmidt, L.-P. 2013, International Journal of Microwave and Wireless Technologies, 5, 49
Kong, S., Arce, H. G., Feddersen, J. R., et al. 2018, ApJS, 236, 25
Krumholz, M. R. & Matzner, C. D. 2009, ApJ, 703, 1352
Langer, W. D. & Penzias, A. A. 1990, ApJ, 357, 477
Leroy, A. K., Walter, F., Brinks, E., et al. 2008, AJ, 136, 2782
Mac Low, M.-M. & McCray, R. 1988, ApJ, 324, 776
Mangum, J. G., Emerson, D. T., & Greisen, E. W. 2007, A&A, 474, 679
McCray, R. & Kafatos, M. 1987, ApJ, 317, 190
McCray, R. & Snow, T. P., J. 1979, ARA&A, 17, 213
McDowell, J. C. 2020, The Astrophysical Journal, 892, L36
McKee, C. F. & Ostriker, J. P. 1977, ApJ, 218, 148
McKinney, W. 2010, in Proceedings of the 9th Python in Science Conference, ed. S. van der Walt & J. Millman, 51 – 56
Megeath, S. T., Gutermuth, R., Muzerolle, J., et al. 2016, AJ, 151, 5
Menten, K. M., Reid, M. J., Forbrich, J., & Brunthaler, A. 2007, A&A, 474, 515
Murray, N., Quataert, E., & Thompson, T. A. 2010, ApJ, 709, 191
Natta, A., Walmsley, C. M., & Tielens, A. G. G. M. 1994, ApJ, 428, 209
Norman, C. A. & Ikeuchi, S. 1989, ApJ, 345, 372
O'Dell, C. R. 2001, ARA&A, 39, 99
O'Dell, C. R., Henney, W. J., Abel, N. P., Ferland , G. J., & Arthur, S. J. 2009, AJ, 137, 367
O'Dell, C. R., Kollatschny, W., & Ferland, G. J. 2017, ApJ, 837, 151
Offringa, A. R., de Bruyn, A. G., Zaroubi, S., et al. 2013, A&A, 549, A11
Okada, Y., Higgins, R., Ossenkopf-Okada, V., et al. 2019, A&A, 631, L12
Oonk, J. B. R., van Weeren, R. J., Salas, P., et al. 2017, MNRAS, 465, 1066
Ossenkopf, V. 2009, A&A, 495, 677
Ossenkopf, V., Röllig, M., Neufeld, D. A., et al. 2013, A&A, 550, A57
Osterbrock, D. E. & Ferland, G. J. 2006, Astrophysics of gaseous nebulae and active galactic nuclei
Pabst, C., Higgins, R., Goicoechea, J. R., et al. 2019, Nature, 565, 618
Pabst, C. H. M., Goicoechea, J. R., Teyssier, D., et al. 2020, A&A, 639, A2
Pabst, C. H. M., Goicoechea, J. R., Teyssier, D., et al. 2017, A&A, 606, A29
Peeters, E., Martín-Hernández, N. L., Damour, F., et al. 2002, A&A, 381, 571
Pence, W. D., Chiappetti, L., Page, C. G., Shaw, R. A., & Stobie, E. 2010, A&A, 524, A42
Pety, J. 2005, in SF2A-2005: Semaine de l'Astrophysique Francaise, ed. F. Casoli, T. Contini, J. M. Hameury, & L. Pagani, 721
Pineda, J. L., Stutzki, J., Buchbender, C., et al. 2020, The Astrophysical Journal, 900, 132
Planck Collaboration, Ade, P. A. R., Aghanim, N., et al. 2011, A&A, 536, A19
Pound, M. W. & Wolfire, M. G. 2008, in Astronomical Society of the Pacific Conference Series, Vol. 394, Astronomical Data Analysis Software and Systems XVII, ed. R. W. Argyle, P. S. Bunclark, & J. R. Lewis, 654
Reynolds, S. P. 2017, Dynamical Evolution and Radiative Processes of Supernova Remnants, ed. A. W. Alsabti & P. Murdin, 1981
Risacher, C., Güsten, R., Stutzki, J., et al. 2016a, A&A, 595, A34
Risacher, C., Gusten, R., Stutzki, J., et al. 2016b, IEEE Transactions on Terahertz Science and Technology, 6, 199
Salas, P., Oonk, J. B. R., Emig, K. L., et al. 2019, A&A, 626, A70
Salas, P., Oonk, J. B. R., van Weeren, R. J., et al. 2017, MNRAS, 467, 2274
Schneider, N., Simon, R., Guevara, C., et al. 2020, Publications of the Astronomical Society of the Pacific, 132, 104301
Spitzer, L. 1978, Physical processes in the interstellar medium
Stacey, G. J., Hailey-Dunsheath, S., Ferkinhoff, C., et al. 2010, ApJ, 724, 957
Stacey, G. J., Jaffe, D. T., Geis, N., et al. 1993, ApJ, 404, 219
Suri, S., Sánchez-Monge, Á., Schilke, P., et al. 2019, A&A, 623, A142
Suri, S. e. a. in prep.
Tielens, A. G. G. M. & Hollenbach, D. 1985, ApJ, 291, 747
Tielens, A. G. G. M., Meixner, M. M., van der Werf, P. P., et al. 1993, Science, 262, 86
Townsley, L. K., Feigelson, E. D., Montmerle, T., et al. 2003, ApJ, 593, 874
Tsivilev, A. P. 2014, Astronomy Letters, 40, 615
Virtanen, P., Gommers, R., Oliphant, T. E., et al. 2020, Nature Methods, 17, 261
Visser, R., van Dishoeck, E. F., & Black, J. H. 2009, A&A, 503, 323
Weaver, R., McCray, R., Castor, J., Shapiro, P., & Moore, R. 1977, ApJ, 218, 377
Williams, J. P. & McKee, C. F. 1997, ApJ, 476, 166
Wolfire, M. G., Hollenbach, D., & McKee, C. F. 2010, ApJ, 716, 1191
Wolfire, M. G., Hollenbach, D., McKee, C. F., Tielens, A. G. G. M., & Bakes, E. L. O. 1995, ApJ, 443, 152
Young, E. T., Becklin, E. E., Marcum, P. M., et al. 2012, ApJ, 749, L17
Zuckerman, B. & Evans, N. J., I. 1974, ApJ, 192, L149

Appendix A: Supplementary material

Flight ID	Tiles	Tile IDs	Spectra count
2016-11-10_GR_F348	2	0505, 0605	34272
2016-11-15_GR_F349	9	0105, 0205, 0304, 0305, 0306, 0307,0405, 0705, 0805	272160
2016-11-16_GR_F350	8	0206, 0301, 0302, 0303, 0406, 0506, 0606, 0706	226800
2016-11-17_GR_F351	8	0106, 0107, 0206, 0207, 0407, 0507, 0607, 0608	226800
2016-11-18_GR_F352	8	0204, 0404, 0408, 0504, 0508, 0604, 0704, 0804	244440
2017-02-08_GR_F371	8	0004, 0104, 0204, 0206, 0503, 0505, 0603, 0605	181440
2017-02-09_GR_F372	10	0003, 0103, 0203, 0403, 0502, 0602, 0603, 0702, 0703, 0803	277200
2017-02-10_GR_F373	5	0102, 0202, 0402, 0501, 0601	138600
2017-02-14_GR_F374	8	0101, 0201, 0401, 0509, 0601, 0609, 0708, 0709	209160
2017-02-15_GR_F375	8	0309, 0310, 0409, 0410, 0509, 0510, 0610, 0710	236880
2017-02-16_GR_F376	7	0311, 0411, 0511, 0611, 0612, 0711, 0712	185220
2017-02-17_GR_F377	9	0308, 0312, 0403, 0412, 0512, 0612, 0703, 0707, 0803	228060
		Total Spectra	2461032

Table A.1: Summary of flights and tiles observed. The project was observed over 13 flights, 12 flights were used for map observing. A separate flight was dedicated to calibration and OFF check observations.

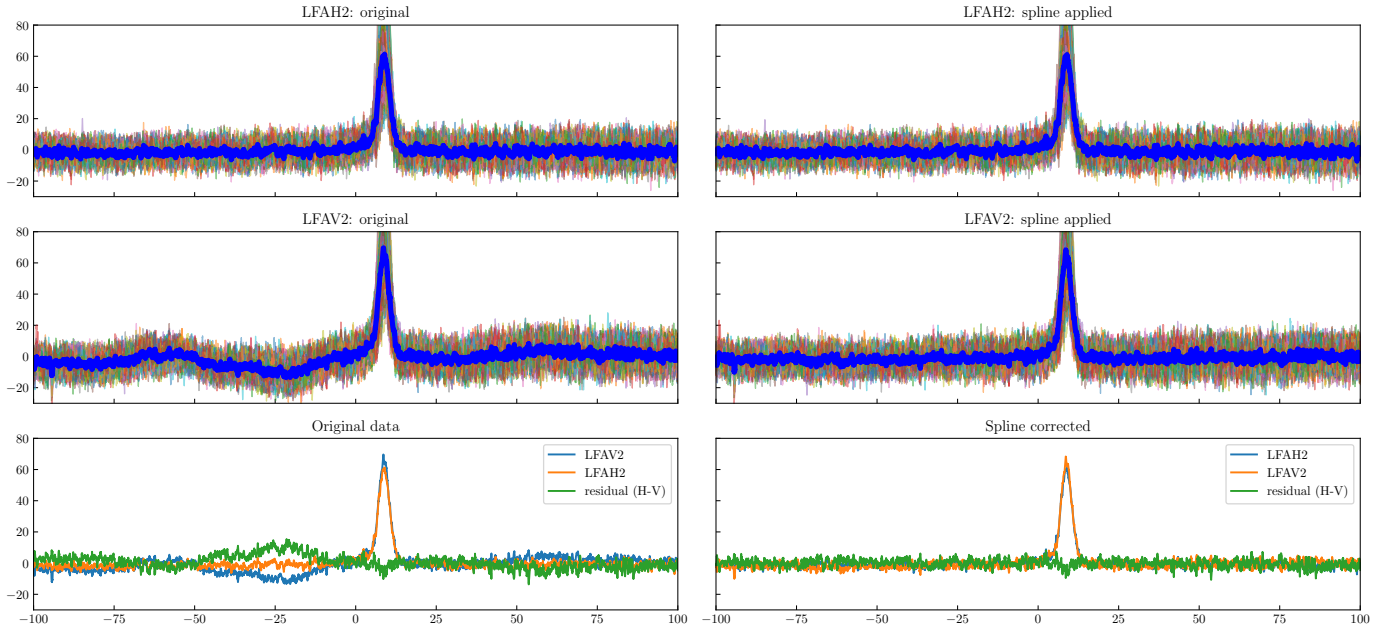

Fig. A.1: Comparison between the LFAH2 (left panels) and LFAV2 (right panels) pixels with and without spline baseline correction. Dark blue lines show the average spectrum over 84 spectra. The lower panels show the residual between the H and V data with and without spline correction. There is a 5 kelvin difference between the peak intensity before and after spline correction, indicating that spline correction has not affected the line intensity. Note that the LFAH2 and LFAV2 aren't co-aligned and are offset on the sky by 2 arcseconds which could account for the different line intensity seen between the 2 detectors.

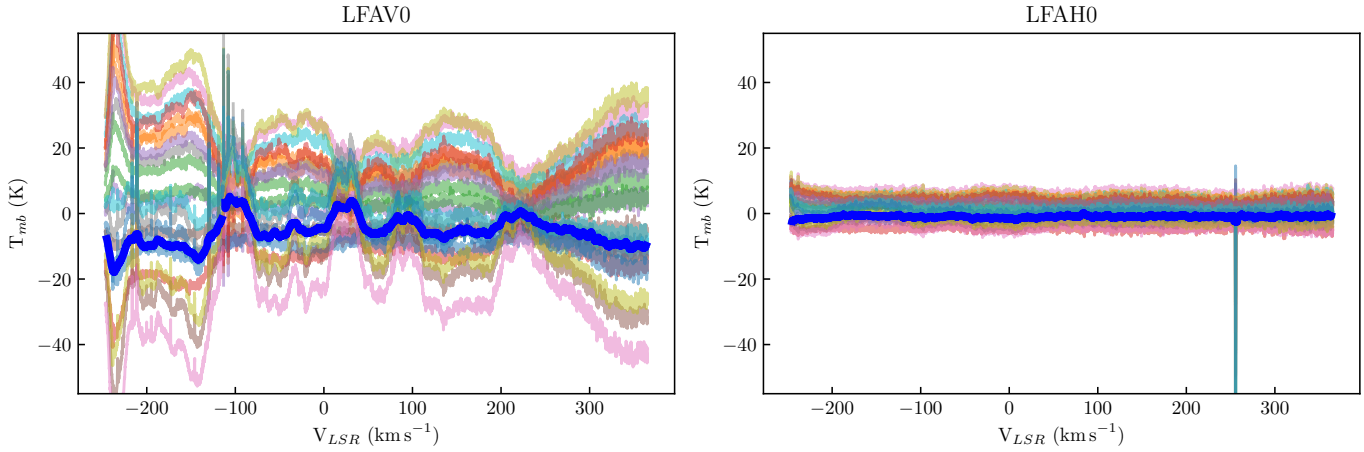

Fig. A.2: Calibrated residual between different OFF measurements taken over a flight leg which is used to generate a catalogue of baseline shapes. Note large residual between LFAV0 pixel (left panel) compared to the more stable pixel LFAH0 (right panel).

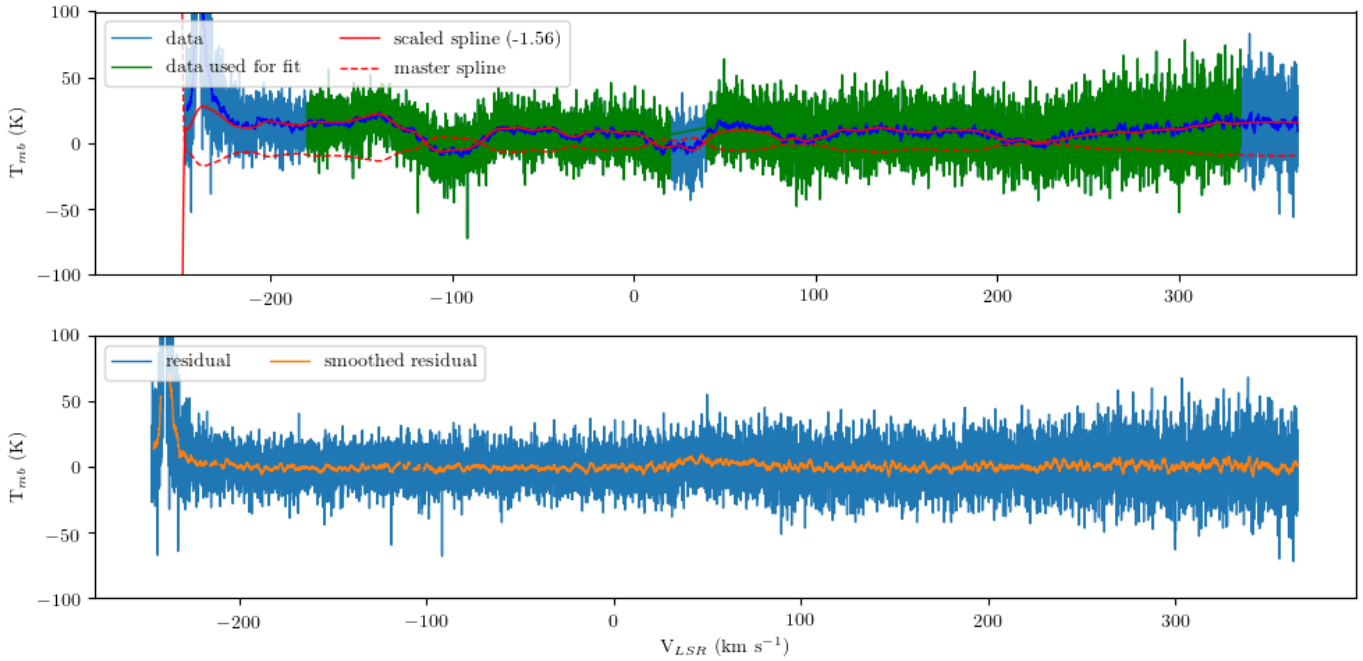

Fig. A.3: Spline correction of a single OTF dump for the Galactic center project. *Upper Panel:* The master spline (shown in a dashed red line) used in the correction is shown in figure A.2 in dark blue. This master spline is scaled by a factor of -1.5 which provides a good match to the original data. *Lower panel:* The residual after scaled spline subtraction. Note weak emission seen between 20 and 70 km s^{-1}in the spline corrected spectrum that is not visible in the original data.

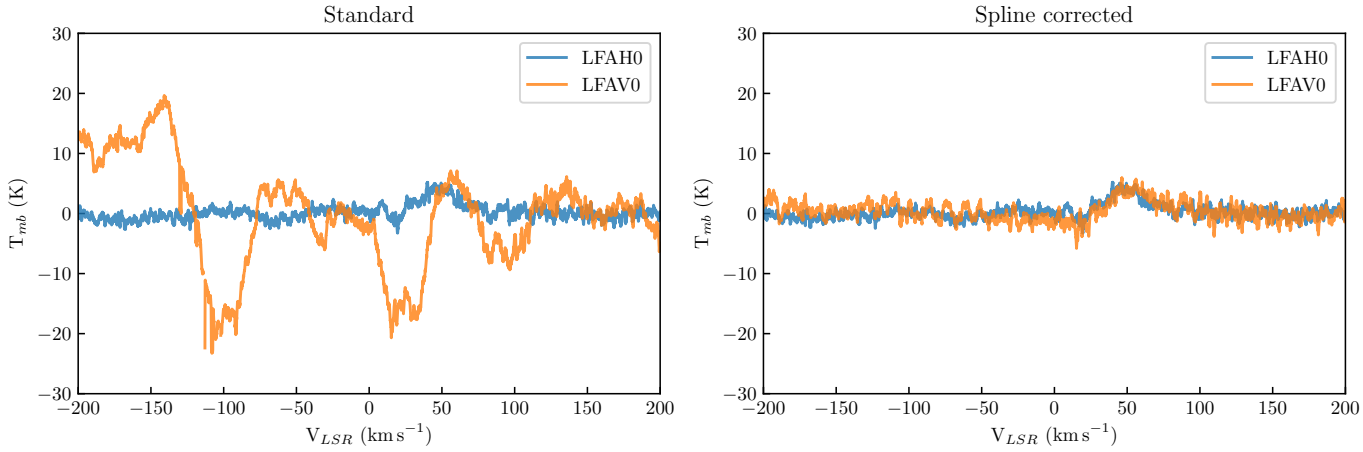

Fig. A.4: Before and after spline correction. Average of 80 spectra from an OTF scan taken as part of the [CII] Galactic center mapping project (data shown in figure A.3 is part of this average). *Left panel:* Standard reduction with a third order polynomial baseline correction. *Right panel:* Reduction using the spline catalogue approach. Note [CII] emission from 20 to 70 km s^{-1} and consistent line emission seen between coaligned (~ 2 arcseconds) H and V pixels after correction.

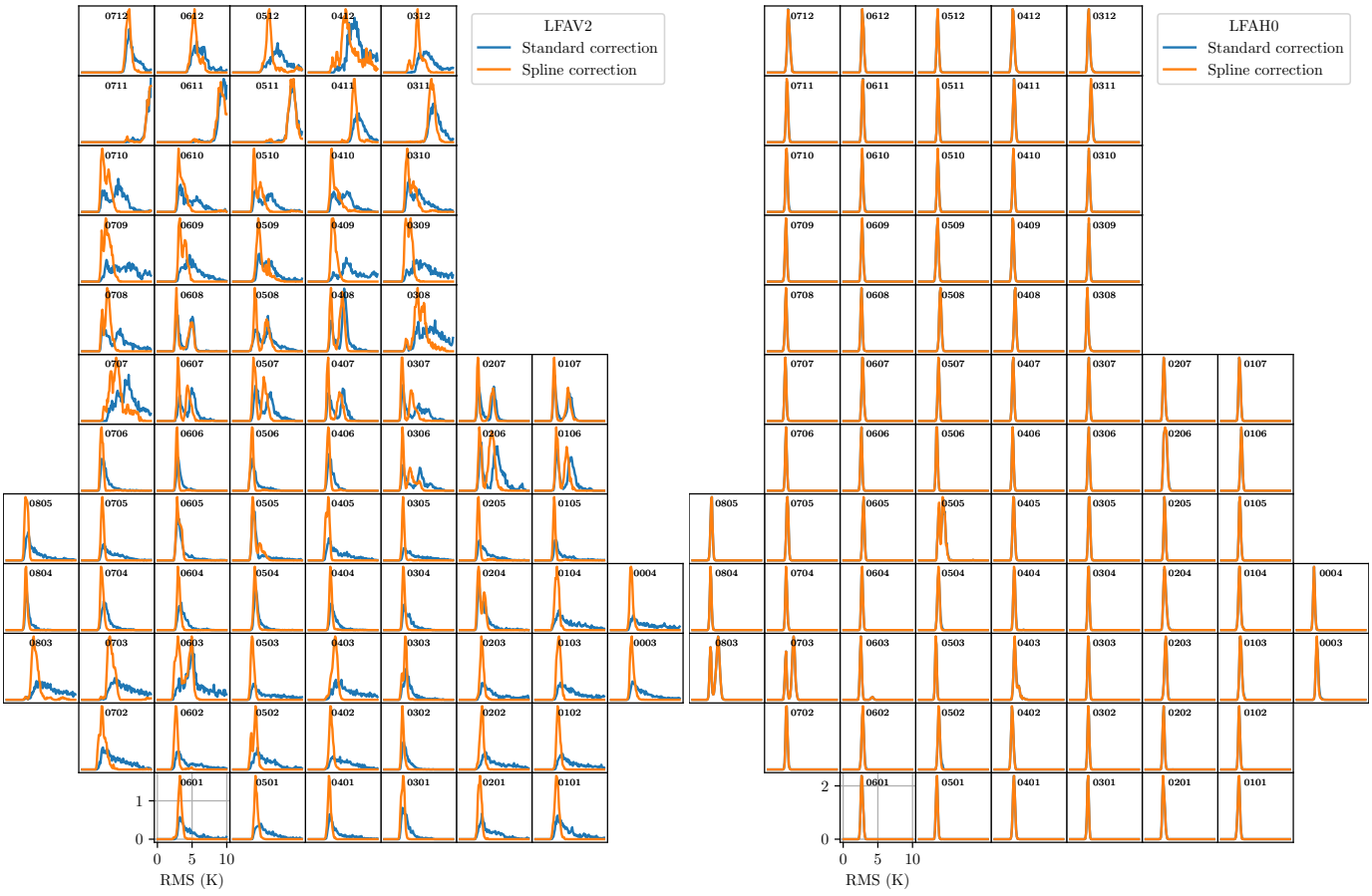

Fig. A.5: Histogram RMS distribution for all spectra for pixel LFAV2 (left panel) and LFAH0 (right panel) per map tile. The RMS distribution is shown before (blue) and after baseline spline correction (orange). Baseline issues in the RMS distribution plot by a large tail towards higher RMS values. Note that LFAV2 pixel shows a noticeably improvement in RMS distribution compared to the standard polynomial baseline correction. Conversely LFAH0 has no baseline performance issue and so the application of the spline correction made no significant difference to the RMS distribution. The RMS is taken over a range of -100 to 100 km/s with the central region from -20 to 30 km/s ignored for the RMS determination, spectra shown have a 0.2 km/s resolution.

Fig. A.6: Summary of upGREAT LFA single sideband receiver temperature over the 13 project flights. Note the increase in receiver temperature for the V array towards later flights that was linked to a degradation in LFAV LO performance. The LO was shipped back to the manufacturer for maintenance after the flight series. The H LO was not available during the 2016-11-10 flight and is recorded here with 0 receiver temperature.

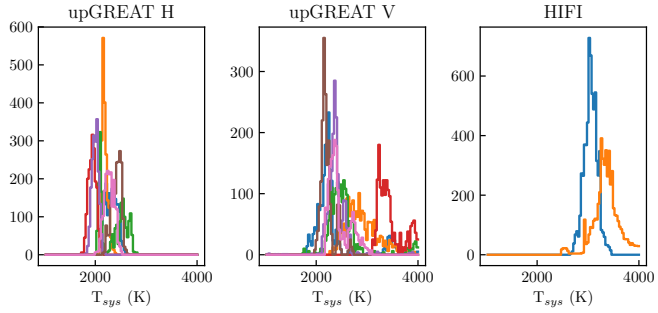

Fig. A.7: Distribution of single side band system temperature for each pixel over all 13 flights with a comparison to HIFI system temperatures for the Orion map. Receiver temperatures shown are measured in the IF band where the astronomical signal is signal. In the case of upGREAT this is at an IF of 1.9 GHz (see figure A.8).

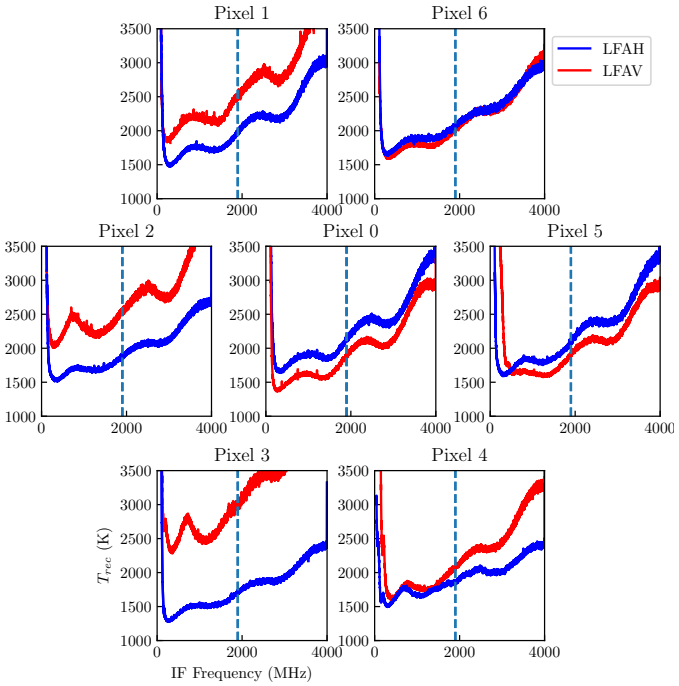

Fig. A.8: Example of upGREAT single sideband receiver temperatures. The IF frequency used to set the LO frequency is marked at 1.9 GHz which corresponds to a V_{LSR} of 10 km/s. Note the slope in receiver temperature increasing towards higher IF frequencies. Lower receiver temperatures are available at lower IF frequencies but they can be susceptible to LO instabilities or spurious output.

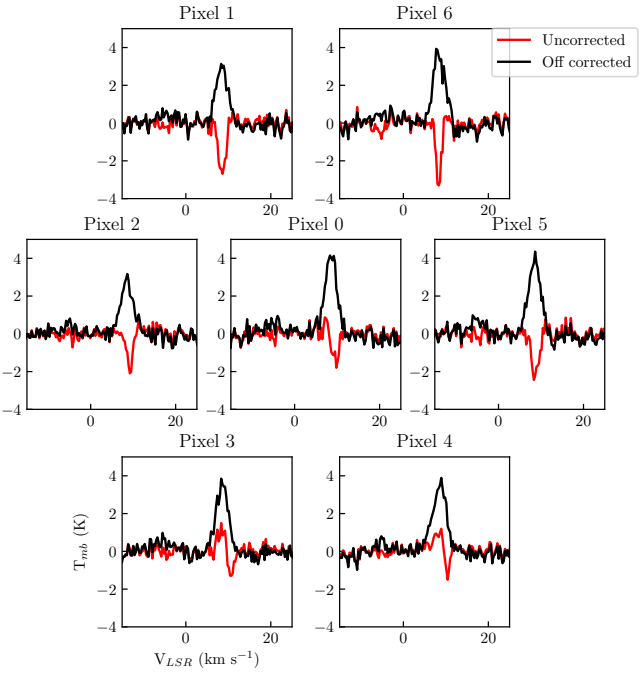

Fig. A.9: Example of OFF correction process for H array showing average emission for tile 0303 before and after correction for OFF contamination from the COFF-C position.

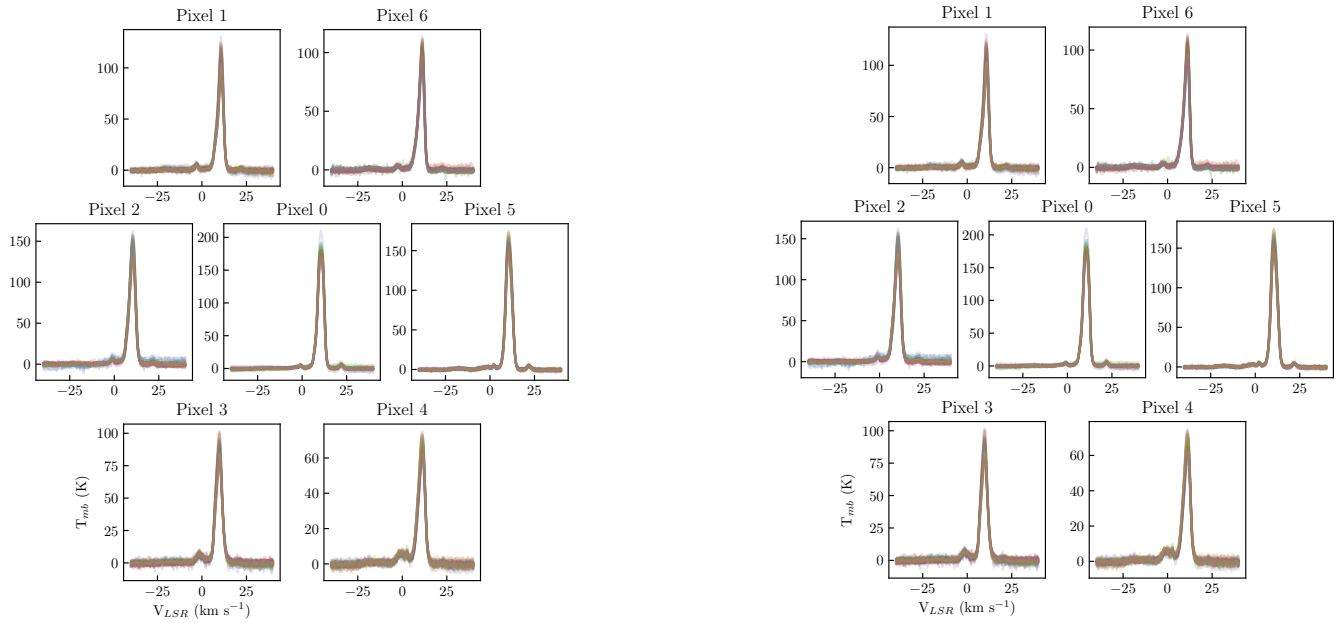

Fig. A.10: Overview plot showing all calibration observations of the Orion bar observed over 13 flights, 20 single point total power observations in total, see section 4.1 for more details. The LFAH array is shown in the left panel, LFAV in the right panel.

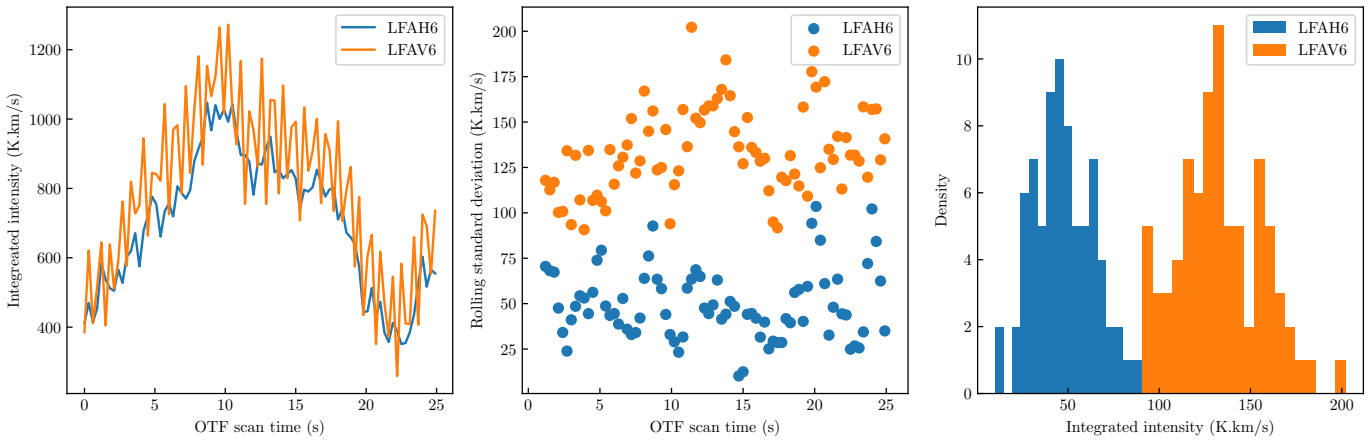

Fig. A.11: Detection of gain instability in an OTF scan using a rolling standard deviation over the integrated intensity of an OTF scan. *Left panel:* Integrated intensity variation over a 25 second OTF scan with 84 spectra. Note larger variation for LFAV6 compared to LFAH6. *Center panel:* Rolling standing deviation over 5 samples. A rolling standard deviation removes the sky signal variation during the OTF scan and leaves just the OTF sample to sample variations. *Right panel:* Distribution of rolling standard deviation. Note the unstable pixel, LFAV6, shows a large mean standard deviation compared to the LFAH6 pixel. This property can be used to detect gain instability in a given pixel.

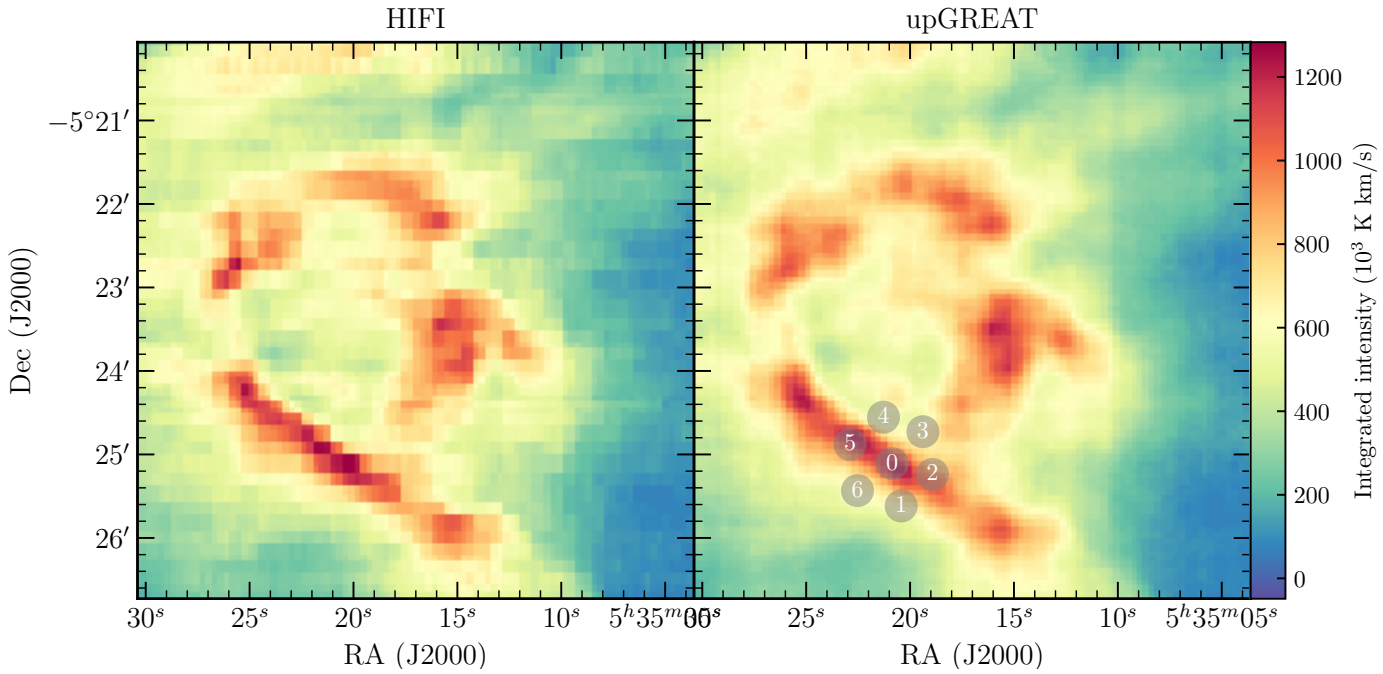

Fig. A.12: Side by side plot of HIFI and upGREAT data gridded with an 18 arcsecond beam. The variation of integrated intensity between -5 and 15 km/s is shown. The array positions highlighted in grey shows the location of the Orion bar consistency observation. The map is generated with a 18.1 arcsecond kernel. Note the smoother map seen for upGREAT showing the difference between a fully sampled (5.2 arcsecond sampled) and the HIFI partially sampled grid (10 arcsecond samples), see figure A.13 for an overview of the OTF dump positions.

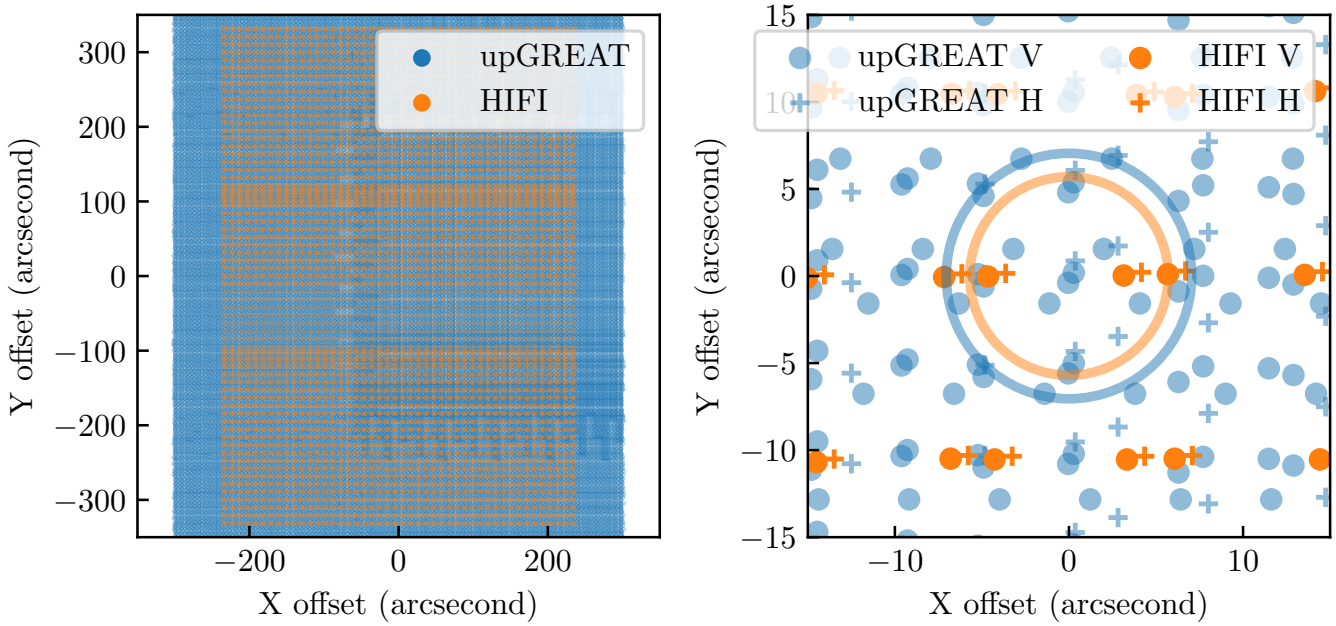

Fig. A.13: *Left panel:* Overview of spectra positions for HIFI and upGREAT maps. *Right panel:* Zoom on central map region. Note sparse sampling of HIFI map with 11 arcsecond spacing between OTF scans, since half the OTF scan is spent observing the internal cold load there are gaps in coverage along the scan direction. HIFI observed in a ABBA format, so we see 2 ON spectra taken in succession followed by 2 load observations. HIFI and upGREAT beam size are over plotted for comparison, 11.4 and 14.1 arcseconds respectively.